Earth's Field Magnetic Resonance Imaging in Urban Environments

Noise Suppression and Advanced Image Reconstruction Techniques

Trinity College Dublin
Coláiste na Tríonóide, Baile Átha Cliath
The University of Dublin

Xinyu Zhang

Supervisor: Dr. Friedrich Wetterling

Department of Electronic and Electrical Engineering
Trinity College Dublin

This dissertaton is submitted in partial fulfillment for the degree of
MSc in Electronic Information Engineering

Trinity College Dublin July 2025

Declaration

I declare that this thesis has not been submitted as an exercise for a degree at this or any other university and it is entirely my own work. It contains nothing which is the outcome of work done in collaboration with others, except as specified in the text and Acknowledgements.

I have read and I understand the plagiarism provisions in the General Regulations of the University Calendar for the current year. I have also completed the Online Tutorial provided by the Library, Trinity College Dublin, on avoiding plagiarism 'Ready, Steady, Write', located at `http://tcd-ie.libguides.com/plagiarism/ready-steadywrite`

I agree to deposit this thesis in the University's open access institutional repository or allow the library to do so on my behalf, subject to Irish Copyright Legislation and Trinity College Library conditions of use and acknowledgement.

Xinyu Zhang
July 2025

Acknowledgements

I would like to express my heartfelt gratitude to my supervisor, Dr. Friedrich Wetterling, Assistant Professor, for his continuous guidance, encouragement, and support throughout my research and the preparation of this thesis. I am especially thankful for his understanding and kindness during a particularly difficult period in my life. His patient guidance and thoughtful advice helped me regain focus and confidence in my academic work, and his genuine concern for my well-being meant a great deal to me. I am deeply grateful to my mother for her unwavering love and support, which have been the foundation of my strength and perseverance throughout this journey. I would also like to thank my grandparents for their constant encouragement and faith in me, which have inspired me to pursue my goals with dedication. Without their support, this thesis would not have been possible.

Abstract

This dissertation investigates the feasibility and practical implementation of Earth's Field Magnetic Resonance Imaging (EF-MRI) under real-world urban noise environments, with experiments conducted at Trinity College Dublin (city centre) and a Dublin suburb. Operating at the Earth's magnetic field (50 μT) with ultra-low Larmor frequencies (1.9 kHz), EF-MRI offers a low-cost, portable alternative to conventional high-field MRI systems, addressing accessibility challenges in resource-limited settings. However, environmental noise, electromagnetic interference, low polarization, and frequency drift remain critical challenges for its practical deployment.

Using the Magritek Terranova EFNMR system, this work conducted imaging experiments on two distinct water bottle phantom samples, employing both the Filtered Back Projection (FBP) method and k-space imaging techniques to evaluate reconstruction performance under different noise environments. To mitigate the impact of environmental noise, the study integrates systematic calibration, including AutoShim for field homogeneity optimization, B1 pulse duration adjustment, and environmental noise mapping, combined with advanced signal processing approaches such as exponential temporal weighting, frequency correction, and k-space filtering.

1D, 2D, and 3D EF-MRI imaging experiments demonstrate successful noise suppression and improved image quality in unshielded environments, achieving enhanced Signal-to-Noise Ratio (SNR) and Structural Similarity Index (SSIM). Comparative evaluations with default Prospa reconstructions further confirm the proposed pipeline's effectiveness in improving spatial resolution, contrast, and structural fidelity.

This work demonstrates that combining system optimization with advanced signal processing enables stable and practical EF-MRI imaging under urban conditions, pro-

viding experimental evidence and methodological insights for the future deployment of low-cost MRI in community-level healthcare.

Keywords

Earth's Field Magnetic Resonance Imaging, Urban Noise Environment, Filtered Back Projection, k-space Imaging,Signal Processing, Image Reconstruction.

Table of contents

List of figures

List of tables

Nomenclature

Roman Symbols

B_0	Static magnetic field strength (Earth's field, ~50 μT)
B_1	Radiofrequency (RF) excitation magnetic field
Δf	Frequency offset / frequency drift
f_0	Larmor frequency under B_0
G	Magnetic field gradient
I	Image reconstructed from IFFT
k	Spatial frequency coordinate in k-space
$\mathcal{K}(k_x, k_y, k_z)$	Acquired k-space data
k_x, k_y, k_z	Spatial frequency axes in k-space
N_x, N_y, N_z	Matrix size along X, Y, Z axes

Greek Symbols

γ	Gyromagnetic ratio (42.58 MHz/T for proton)
σ	Standard Deviation

Subscripts

$_{\text{filtered}}$ After filtering

k k-space (frequency domain) axis

$_{\text{padded}}$ After zero-padding

$_{\text{raw}}$ Raw (unprocessed) data

$_{\text{ref}}$ Reference scan / phantom

t Time domain

x, y, z Spatial axes

Acronyms / Abbreviations

EF-MRI Earth's Field Magnetic Resonance Imaging

FFT Fast Fourier Transform

FID Free Induction Decay

FOV Field of View

IFFT Inverse Fast Fourier Transform

MRI Magnetic Resonance Imaging

NMR Nuclear Magnetic Resonance

PCA Principal Component Analysis

RF Radio Frequency

SNR Signal-to-Noise Ratio

SSIM Structural Similarity Index

T_1 Longitudinal relaxation time

T_2 Transverse relaxation time

T_2^* Effective transverse relaxation time (includes field inhomogeneity)

TE Echo Time

TR Repetition Time

CHAPTER 1

Introduction

1.1 Background

MAGNETIC Resonance Imaging (MRI) has become an indispensable tool in clinical diagnosis, neuroscience research, and biomedical engineering. Its non-invasive, non-ionizing nature and capacity for multiparametric imaging have made it a cornerstone in diagnostics, disease prognosis, and interventional planning. However, the conventional MRI systems rely on large superconducting magnets, making them costly, bulky, and infrastructure-dependent. This limits their accessibility, particularly in low-resource settings such as rural hospitals, mobile diagnostics, or developing countries.

Magnetic Resonance Imaging (MRI) has, since its introduction in 1973 [3], revolutionized medical diagnostics, neuroscience, and therapeutic monitoring, becoming a critical pillar of modern clinical practice [8]. MRI's ability to produce high-resolution, non-invasive images of soft tissue has contributed significantly to advancing global health. Reflecting its profound societal impact, the foundational work in Nuclear Magnetic Resonance (NMR) and MRI has garnered multiple Nobel Prizes over the past seven decades [9].

However, access to MRI technology remains unevenly distributed across the globe. In 2008, the World Health Organization (WHO) reported that approximately 90% of the global population lacked access to MRI [10]. Although more recent reports show improvements in scanner density in emerging economies, these advancements remain significantly below levels observed in high-income OECD nations [11].

The primary reasons for this disparity are rooted in the conventional focus of MRI development: achieving maximum image quality and performance. This emphasis has driven up costs and complexity, placing MRI out of reach for many low- and middle-income countries (LMICs) due to infrastructural limitations, lack of skilled personnel, and high maintenance burdens [12]. For example, in sub-Saharan Africa, the scanner density is often below 0.1 per million people, with some countries having none at all [13][14]. Similarly, the Indian subcontinent, despite its large population, continues to face heterogeneous access, particularly in rural and underserved areas [15].

This lack of accessibility is not merely a technological or economic issue; it has significant public health implications. MRI plays a pivotal role in the early detection and management of diseases such as cancer, stroke, and neurodegenerative disorders. Inaccessible or delayed diagnostics can lead to poor health outcomes and increased healthcare costs. Thus, reducing global inequities in MRI availability is a critical step toward achieving equitable healthcare.

In response to these challenges, a new frontier in MRI research has emerged: low-field and ultra-low-field MRI (LF-MRI and ULF-MRI). Operating at magnetic field strengths several orders of magnitude below clinical systems, these technologies aim to drastically reduce system complexity and cost while maintaining clinically relevant imaging capabilities [16]. One especially promising variant is Earth's Field MRI (EF-MRI), which uses the Earth's magnetic field ($\sim$50 μT) for signal detection. While the signal-to-noise ratio (SNR) is inherently lower, EF-MRI significantly reduces reliance on superconducting magnets and associated cryogenic systems, allowing for simpler, mobile, and low-power platforms [17].

Moreover, EF-MRI offers unique compatibility with urban and resource-limited environments. Studies have demonstrated that despite the challenges posed by ambient electromagnetic noise and field inhomogeneity, robust imaging is possible with adequate signal processing and shielding-free designs [18]. These advances underscore the feasibility of using EF-MRI for community-level diagnostics and point-of-care applications in low-resource settings.

From a policy perspective, enhancing MRI accessibility aligns with WHO's five-dimension framework for medical device access: geographical, temporal, financial, cultural, and digital [19]. EF-MRI, by virtue of its low-cost, portable, and low-maintenance nature, addresses several of these dimensions simultaneously. It represents not merely a technical innovation, but a strategic shift toward democratizing medical imaging and bridging the global diagnostic divide.

In summary, the development of accessible MRI modalities like EF-MRI is both a scientific opportunity and a moral imperative. Addressing the limitations of conventional high-field systems and expanding diagnostic capabilities to underserved populations will require coordinated efforts in engineering, policy, training, and deployment. The work presented in this dissertation contributes to this broader mission by advancing practical methods for improving EF-MRI image quality in noisy urban environments, thus paving the way for its real-world implementation.

1.2 Problem Description

Despite its theoretical promise, EF-MRI remains significantly constrained in practice. Operating at ultra-low Larmor frequencies (1.9 kHz), EF-MRI is inherently more vulnerable to electromagnetic interference (EMI), low thermal polarization, and environmental noise compared to high-field MRI systems. These limitations lead to degraded signal stability, spectral overlap, and compromised spatial resolution. In urban settings, ambient EMI—such as power line harmonics at 50 Hz—further exacerbates signal degradation, challenging the clinical or diagnostic utility of EF-MRI systems.

Preliminary experiments conducted with the Magritek Terranova EFNMR platform in Dublin, Ireland, confirm these concerns. Severe SNR limitations, frequency drift, and image blurring were observed in unshielded conditions, highlighting the urgent need for systematic hardware calibration, advanced noise suppression, and improved image reconstruction techniques tailored to EF-MRI's constraints. Therefore, this project aims to bridge the gap between theoretical feasibility and practical deployment by combining experimental system tuning with computational signal enhancement methods.

1.3 Research Objectives

The overarching aim of this project is to investigate the feasibility and real-world applicability of Earth's Field Nuclear Magnetic Resonance (EFNMR) as a cost-effective and portable imaging modality, particularly under urban environmental conditions where conventional MRI systems are impractical or inaccessible. This study focuses on optimizing signal acquisition and reconstruction workflows, improving the signal-to-noise ratio (SNR), and developing robust post-processing strategies to enhance image quality in the presence of noise and hardware limitations.

1. System Setup and Data Acquisition

- Optimize system parameters such as B1 frequency and RF pulse duration to ensure robust and reproducible signal excitation.
- Enhance Free Induction Decay (FID) quality through precise coil tuning, calibration of B1 pulses, and reduction of system and environmental noise.

2. Signal Analysis and Noise Characterization

- Analyze raw EFNMR data in controlled (e.g., water-filled phantom) and uncontrolled environments to isolate dominant noise components—particularly 50 Hz line noise.
- Quantify signal integrity through SNR estimation, frequency spectrum analysis, and statistical modeling using MATLAB-based tools.

3. EF-MRI Imaging Experiments

- Conduct 1D, 2D, and 3D imaging experiments under Earth's magnetic field using phantom-based test objects.
- Evaluate projection-based reconstructions across different orientations and optimize acquisition parameters to maximize imaging fidelity.

4. Post-processing and Image Enhancement

- Apply a variety of post-processing methods, including filtering, frequency correction, and contrast enhancement techniques, to improve image quality.
- Implement and compare multiple image reconstruction strategies such as Filtered Back Projection (FBP), Spin-Echo-based reconstruction, and Gradient Echo imaging to optimize spatial resolution and noise resilience.

5. Performance Evaluation and Benchmarking

- Compare EF-MRI results against conventional MRI outputs or theoretical expectations to assess trade-offs in spatial resolution and diagnostic value.
- Validate experimental results through both qualitative image inspection and quantitative metrics such as root mean square error (RMSE) and normalized mutual information (NMI).

CHAPTER 2

Literature Review

2.1 Structure of Literature Review

The literature review is divided into seven sections that collectively trace the historical evolution, technological innovations, and emerging directions of Earth's Field Nuclear Magnetic Resonance (EFNMR) and Earth's Field Magnetic Resonance Imaging (EF-MRI).

2.2 Early Applications of EFNMR

Magnetic Resonance (EFNMR), though significantly less sensitive than high-field NMR, has roots nearly as old as NMR itself. Packard and Varian [20](1954) first proposed using Earth's magnetic field to detect nuclear precession, laying the theoretical foundation for EFNMR-based instrumentation. Their work demonstrated that when a polarizing magnetic field is abruptly turned off, the residual magnetization in a sample (such as water) precesses around the Earth's magnetic field, generating an oscillating voltage in a nearby detection coil. The frequency of this precession is directly proportional to the magnetic field strength via the gyromagnetic ratio of the proton.

While EFNMR found early applications in geomagnetism and magnetometry (Fig. 2.1), especially in absolute field measurement using proton magnetometers, its potential for medical imaging was long overlooked due to significant limitations in sensitivity and spatial resolution. In particular, the susceptibility of proton precession frequency to

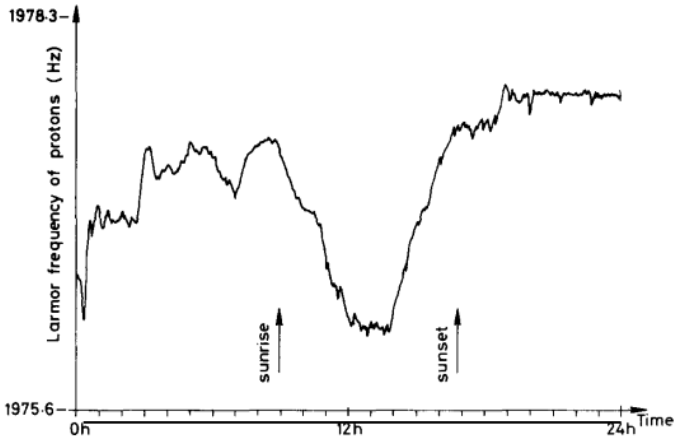

Fig. 2.1 The diurnal variation of the earth field [1]

minute environmental variations—such as those arising from urban magnetic noise or power-line harmonics—has historically posed a critical barrier to EF-MRI image quality.

One critical challenge is the instability of the Larmor frequency under Earth's field [2, 21], especially in urban or unshielded environments, where magnetic field drift and 50 Hz harmonics distort the Free Induction Decay (FID) signal. To address this, Denisova et al.[1] later investigated the influence of such magnetic field variations on proton magnetometer measurements, highlighting how free induction decay (FID) signals are affected by linear, parabolic, or harmonic field changes (Fig. 2.2). They emphasized the necessity of algorithmic averaging and filtering strategies to correct for these frequency distortions—insights that now form the theoretical basis for noise-suppression in modern EF-MRI systems.

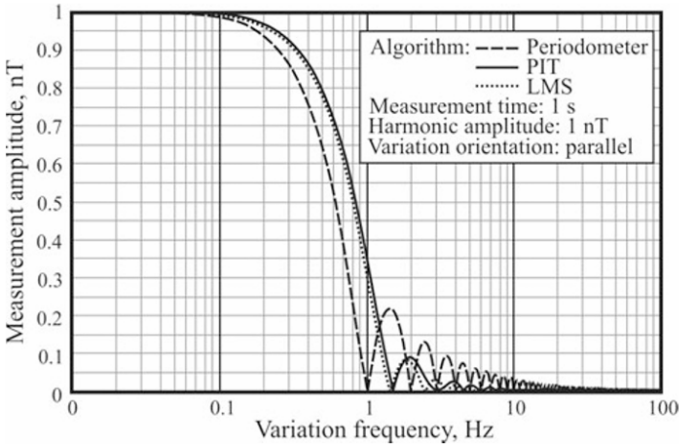

Fig. 2.2 Transient function of the algorithms [2]

2.3 Evolution of Magnetic Resonance Imaging Techniques

While high-field Nuclear Magnetic Resonance (NMR) has long been recognized for its ability to reveal intricate interactions between nuclear spins and their surrounding molecular environments via its detailed spin Hamiltonian, early developments in the 1970s significantly expanded its utility. Lauterbur and Mansfield demonstrated that by spatially varying the magnetic field, NMR could be employed not only for molecular diffusion measurement but also for non-invasive imaging—paving the way for modern Magnetic Resonance Imaging (MRI) techniques [3, 22].

Lauterbur introduced the concept of spatially encoding NMR signals via magnetic field gradients, enabling the reconstruction of two-dimensional images from projection (Fig 2.3) data—essentially laying the foundation of MRI as we know it today (Fig 2.4).

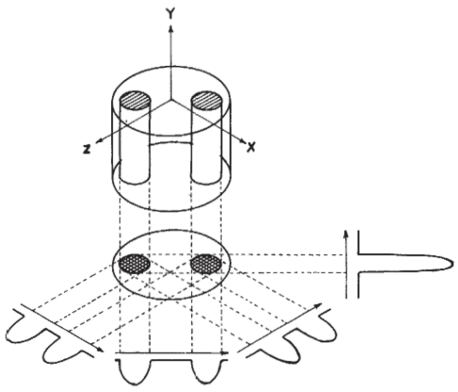

Fig. 2.3 3D Object Relationship [3]

Fig. 2.4 Proton NMR Imaging [3]

Mansfield further refined this approach by introducing echo-planar imaging and mathematical formalisms for image formation. These techniques revolutionized the field of diagnostic imaging, transforming NMR from a tool for chemical and molecular analysis into a non-invasive imaging modality with broad clinical relevance.

While these early advances largely focused on high-field systems, they indirectly highlighted the potential flexibility of NMR physics—even at lower fields. Importantly, they demonstrated that spatial encoding, diffusion sensitivity, and phase manipulation could theoretically be adapted to weaker magnetic environments, thus inspiring later generations of EFNMR and EF-MRI research.

However, despite these breakthroughs, Earth's Field Nuclear Magnetic Resonance (EFNMR)—an ultra-low-field counterpart requiring no superconducting magnets—remained relatively unexplored throughout the ensuing decades. This was primarily due to its weak signal strength and high susceptibility to ambient noise, which posed formidable technical barriers for practical imaging.

It is only in recent years that renewed interest has emerged, with researchers demonstrating that EFNMR, under suitable experimental configurations, can support a broader range of applications than previously imagined. From field-resilient magnetometry to low-cost portable imaging, global efforts have increasingly focused on overcoming EFNMR's sensitivity constraints and environmental instability.

2.4 Pioneering Work in EF-MRI

A milestone in EFNMR imaging was marked by Stepišnik et al.[23], who demonstrated one of the earliest attempts to reconstruct magnetic resonance images using the Earth's magnetic field(Fig 2.5, Fig 2.6) . Their study aimed to bypass the technical and economic burden of large superconducting magnets by developing a low-cost NMR system based entirely on terrestrial magnetism. Despite the field strength being nearly 10,000 times weaker than in conventional MRI, they achieved usable signal-to-noise ratios through prepolarization and careful shielding. Stepišnik's team proposed a two-stage field switch-

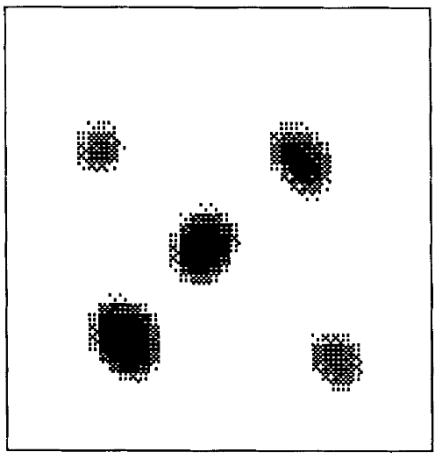

Fig. 2.5 MRI of 4 tubes

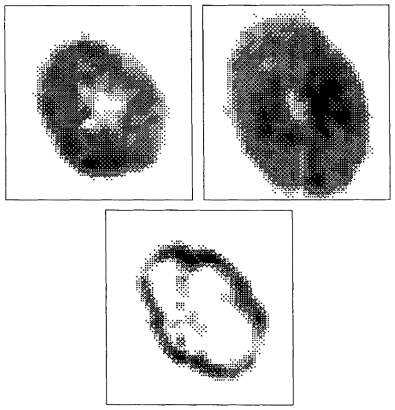

Fig. 2.6 Cross-Sectional Views of a Pear, Apple, and Green Peppe [4]

ing mechanism: a relatively slow adiabatic decay to 10 G, followed by a fast nonadiabatic cutoff, allowing the generation of transverse magnetization in the Earth's field. Using gradient-encoded imaging and Fourier reconstruction, they obtained cross-sectional phantom images with a resolution of approximately 2 mm. Although signal clarity was limited by external noise and system bandwidth, this work laid the groundwork for subsequent portable, low-field MRI systems.

Progress continued in 1990, when Stepišnik's [4] team implemented advanced coil design and noise shielding techniques(Fig 2.7) that improved imaging capabilities in

low-field environments. These developments enabled the acquisition of basic images, although challenges in resolution and signal-to-noise ratio remained.

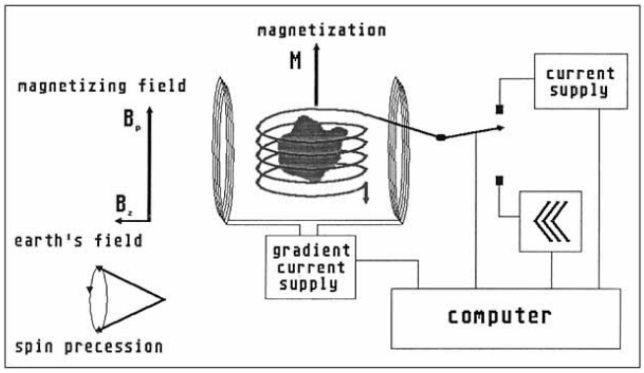

Fig. 2.7 EF-NMR System [4]

However, the equipment and methods are overly complex, posing significant challenges in terms of construction, calibration, and operational stability. In addition, the sensitivity of the system to small magnetic field variations exposes its limitations in field applications where environmental conditions are uncontrollable.

2.5 3D Earth-Field MRI

The evolution of three-dimensional Earth's Field Magnetic Resonance Imaging (3D EF-MRI) began with the work of Halse et al. [5], who presented a practical and flexible implementation of full volumetric imaging in the Earth's magnetic field using a compact laboratory setup. Their system featured a three-axis gradient coil assembly providing both imaging gradients and first-order shimming(Fig 2.8, Fig2.9), enabling sub-Hertz linewidths ($\sim 0.3\,\text{Hz}$) even in indoor environments affected by local field inhomogeneities. A crude pre-polarization coil enhanced the signal-to-noise ratio (SNR), and a surrounding shield mitigated ultra-low-frequency (ULF) environmental noise. This implementation successfully acquired volumetric images of red pepper with an isotropic field-of-view of 160 mm and a matrix size upsampled to 64^3—demonstrating that EF-MRI can function reliably under typical laboratory conditions.

Building on this, Zotev et al. [6] developed a seven-channel SQUID-based 3D ULF MRI and MEG system, which employed pre-polarization (~40 mT) and a SQUID array to image a preserved sheep brain at a 46 μT measurement field. The system achieved a $2.5 \times 2.5 \times 5\,\text{mm}^3$ resolution using 3D Fourier imaging and multi-channel sensitivity encoding (PILS), with image acquisition taking approximately 3 hours. This work demonstrated anatomical

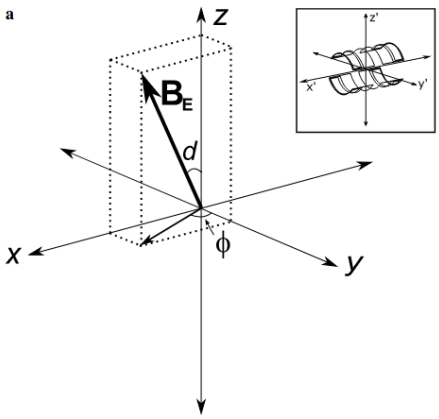

Fig. 2.8 Gradient coil frame

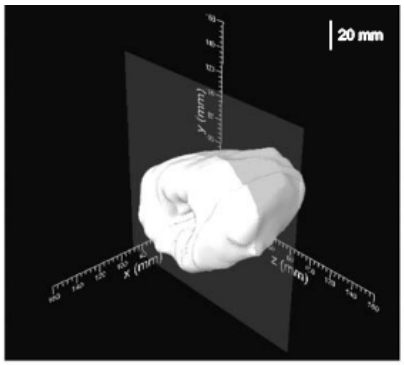

Fig. 2.9 3D MRI of a red capsicum by Halse [5]

detail comparable to 2 T high-field MRI while illustrating the potential of SQUID arrays for parallel imaging in ULF conditions.

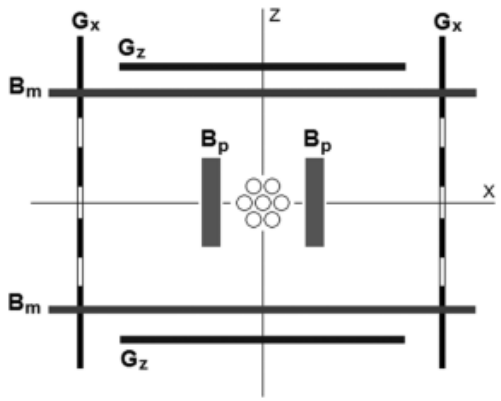

Fig. 2.10 Schematic of the coil system for 2D ULF MRI measurement

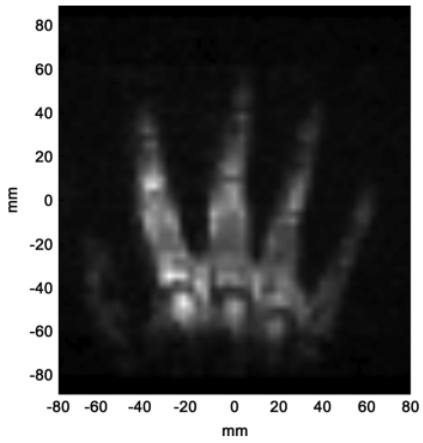

Fig. 2.11 ULF MRI image of a human hand [6]

A notable contribution to the advancement of 3D EF-MRI systems is the compact and rotatable gradient system proposed by Lother et al.[24]. Traditional EF-MRI setups rely on fixed gradient coil geometries designed to function with a static Earth's magnetic field direction. However, such configurations are limited in flexibility and hinder the ability to encode images along multiple orientations. To overcome this, Lother and colleagues engineered a cylindrical gradient system capable of physical rotation with respect to the Earth's magnetic field (B_0), enabling spatial encoding in both parallel and perpendicular configurations.

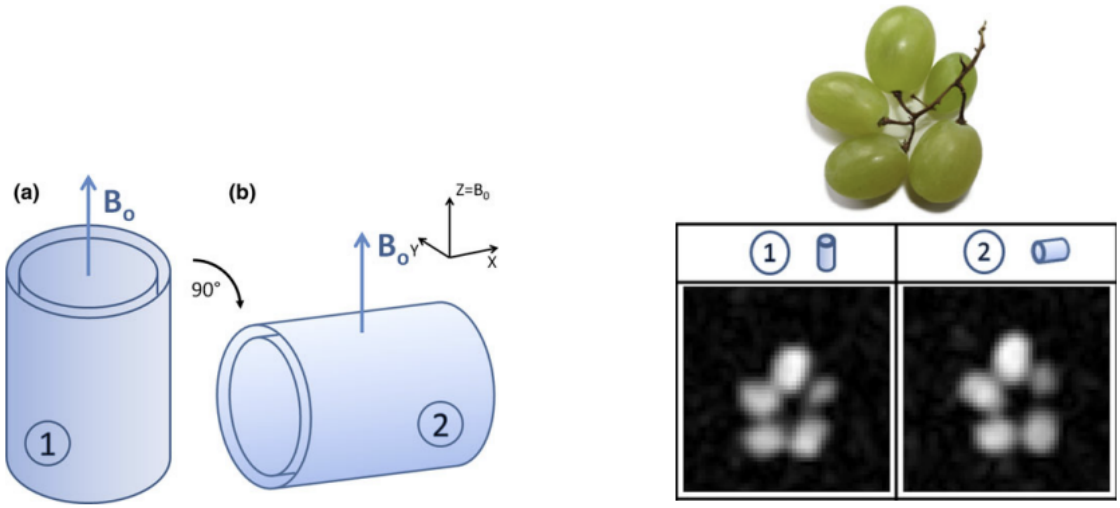

(a) Orientation of the cylindrical gradient system

(b) 2D projection images of grapes measured in the two orientations

Fig. 2.12 Illustrations from Lother et al. (2013) demonstrating the rotatable gradient design and encoding performance under varying B_0 orientations.

The system consists of four independently driven coils—S1 through S4—designed using a combination of Maxwell and Golay geometries. Through the strategic use of concomitant gradients, i.e., the inherent orthogonal components of the generated magnetic field, the system minimizes the number of coils required while preserving full 3D encoding capability. The theoretical framework, derived from Maxwell's equations, was validated through numerical simulations and experimental field mapping. Imaging results, including projections of biological samples like grapes, demonstrated consistent image quality across rotational configurations—proving that a single, rotatable gradient system can effectively support multiple B_0 orientations without requiring reconfiguration.

This approach not only simplifies EF-MRI hardware but also enhances adaptability in environments where the orientation of the Earth's field or the imaging system may vary. Compared to prior multi-coil or static designs, the Lother et al. setup presents a major milestone in the development of field-agnostic EF-MRI instrumentation.

More recently, Liu et al.[18] proposed a 0.055 T ULF-MRI system that operates without an RF shielding room. By integrating a network of EMI sensors and employing a convolutional neural network (CNN) for real-time electromagnetic interference prediction and removal, the system achieved stable imaging performance in unshielded environments. It supports clinical-grade brain imaging and includes standard sequences such as T1W, T2W, FLAIR-like, and DWI, significantly enhancing the utility and sensitivity of ULF-MRI. While Cooley's work centers on hardware portability, Liu's approach highlights system in-

telligence and environmental adaptability, together illustrating the potential of ULF-MRI to evolve toward "shielding-free" and "deep learning–driven" imaging.

Together, these milestones illustrate the progressive trajectory from early EF-MRI systems to robust, volumetric 3D imaging platforms, driven by innovations in gradient hardware, multi-channel detection, pre-polarization, and computational imaging pipelines. Remaining challenges include optimizing acquisition time, SNR, and motion artifact mitigation, as well as transitioning toward clinical validation.

2.6 EFNMR for Environmental and Scientific Research

As demonstrated by the Hahn echo [25] and CPMG echo sequences [26], it became evident that EFNMR could be utilized as a tool for measuring spin (T2) relaxation and molecular diffusion. This concept led to the development of an EFNMR instrument for modeling the role of Antarctic sea ice in global climate and ecology[27, 28].

Due to the unique environmental characteristics of Antarctica, the experiments are not highly reproducible and the detection equipment is complicated, which limits their potential for practical applications.

The imaging system evolved to incorporate a full 3D gradient set and enable magnetization manipulation with audio frequency (AF) oscillating magnetic pulses after 1982. Mobility is another important factor, because the EFNMR apparatus requires no magnet and because everything on Earth is immersed in its field and potentially subject to its influence.Its portability led to unique studies of diffusion in Antarctic ice [29, 30] and groundwater exploration [31, 32].

In parallel with these technological advancements, there is a growing demand for compact, portable, and cost-effective diagnostic instruments, which is driving a paradigm shift in MRI accessibility. This trend aims to democratize MRI by making it available to a much broader population of potential patients. Beyond clinical applications, portable MRI systems have shown great promise in education, facilitating the training of students in engineering, radiology, and biomedical sciences. They also hold potential for basic and applied research, as well as industrial applications. Notably, the emergence of several low-field MRI companies underscores this shift. For example, Hyperfine developed the first FDA-cleared low-field brain scanner [33], while Neuro42 (USA), DeepSpin (Germany), and PhysioMRI (Spain) are advancing specialized low-field MRI systems for head and extremity imaging.

2.7 SNR and Resolution Challenges

Similar signal-to-noise ratio (SNR) reduction and limited spatial resolution are well-documented challenges in X-nuclei MRI, such as ^{23}Na, ^{31}P, and ^{13}C imaging, due to their lower gyromagnetic ratios and in vivo concentrations compared to proton MRI. For instance, Wetterling et al. [34, 35] demonstrated that dedicated coil designs, such as double-tuned ^{1}H/^{23}Na dual resonator systems and asymmetric birdcage resonators, are essential to overcome the inherently low SNR in ^{23}Na MRI, while ultra-short TE sequences are required to capture rapidly decaying sodium signals and mitigate resolution loss. Despite these optimizations, achieving high SNR and sufficient resolution within reasonable scan times remains a limiting factor for X-nuclei MRI, similar to the challenges encountered in ultra-low field proton MRI.

2.8 Overcoming Sensitivity Limitations in Low-Field MRI

The primary challenge limiting the demand for low-field MRI lies in the weak equilibrium polarization of nuclear spins, which scales proportionally with the strength of the magnetic field. This limitation can, however, be overcome through advanced techniques such as dynamic nuclear polarization (DNP) [36–38], optical pumping[39], or pre-magnetization [20]. For larger samples, sensitivity can also be enhanced by increasing the number of turns in the detection coil.

However, signal amplitude in Faraday coil detection remains constrained by magnetic field strength. To overcome this, superconducting quantum interference devices (SQUIDs) [40, 41] have been employed since the 1980s for enhanced sensitivity. SQUIDs, which are sensitive to magnetic flux rather than flux rate changes, provide broadband detection even at ultra-low frequencies without sacrificing sensitivity. Early SQUID-based NMR measurements focused on solid-state samples at liquid helium temperatures, but more recent studies have demonstrated imaging capabilities at room temperature, including spectra from animal tissues and proton samples in microtesla fields [42, 43]. Notably, pre-magnetization in fields of 100–500 mT has enabled the acquisition of two-dimensional proton MR images of water and oil phantoms, cross-sectional views of fruits, three-dimensional (3D) phantoms, and in vivo images of human limbs, which a versatile EF-MRI system equipped for multiple functions, including relaxation time measurement, spectroscopy and imaging in different environments. This multi-functional setup significantly expanded the scope of EF-MRI applications, positioning it as a valuable tool not only for scientific research but also for industrial applications.

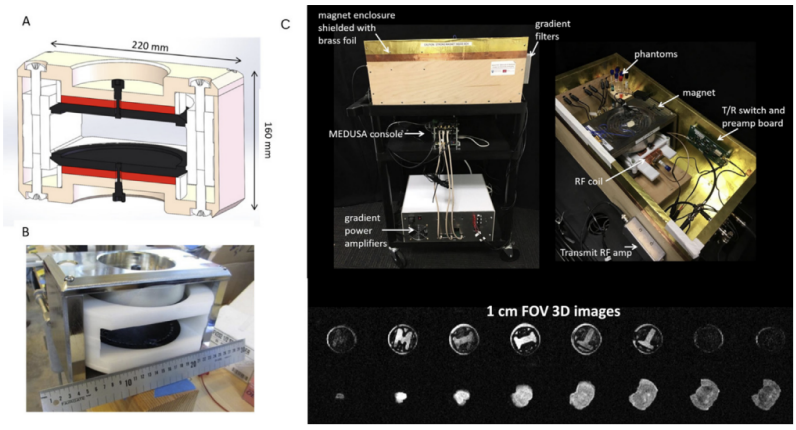

Fig. 2.13 System Overview adapted from Michal's team

Despite the common perception that NMR and MRI require expensive equipment and institutional investment, Michal's team [44] has demonstrated that a wide range of NMR and MRI applications are feasible using low-cost, low-field systems constructed with inexpensive and easily available components, making them accessible for education, prototyping, and research environments. By leveraging microcontrollers, software-defined radios, and low-field magnets including Earth's field and permanent magnets, they successfully implemented low-cost spectrometers and imaging systems with frequencies up to 200 kHz and demonstrated advanced experiments (Fig. 2.13), such as inhomogeneous magnetization transfer (ihMT) imaging using a home-built system assembled during the COVID-19 lockdown. These systems achieved notable SNR and imaging capability improvements by careful coil design and the use of straightforward analog and digital electronics, significantly reducing the barriers to entry for NMR and MRI experimentation outside of high-field laboratories.

Such advancements highlight the potential of low-field, low-cost MRI not only for academic and teaching laboratories but also for exploring novel imaging contrasts and phenomena at ultra-low field strengths, where the interplay of dipolar and Zeeman interactions becomes significant. The feasibility of studying ihMT and other advanced NMR phenomena at low fields using inexpensive hardware provides a promising avenue for expanding MRI accessibility and enabling novel scientific investigations in constrained environments.

Now, low-field magnetic resonance imaging has found applications in medical imaging, such as lung imaging with polarized gases[45], and in industrial fields such as geophysics [46], chemical processing [47–50], and hazardous materials monitoring [51] which indicate that the potential of EF-MRI remains largely untapped.

CHAPTER 3

EF-MRI Methodology

3.1 System Architecture of Low-Field NMR Imaging

3.1.1 Overview of the EF-MRI Acquisition System

The Terranova EFNMR system (Magritek Ltd., New Zealand) utilized in this study adopts a coaxial, multi-coil probe architecture, specifically engineered for signal excitation and detection under ultra-low field conditions. The probe integrates three functionally distinct and concentrically arranged solenoids: (i) a pre-polarization coil, (ii) a tri-axial gradient coil assembly, and (iii) a radiofrequency (B_1) coil. These coils are mechanically interlocked via a bayonet-slot configuration to ensure structural stability and alignment of field geometries, while preserving electromagnetic decoupling between modules.

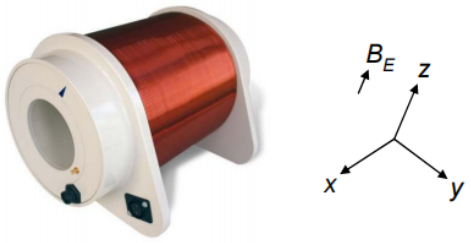

Fig. 3.1 The Earth's Field NMR Probe and axis conventions

The full coil specification is summarized in Table 3.1. This coaxial configuration enables precise spatial superposition of B_0, gradient, and B_1 fields, while maintaining

mechanical robustness and high geometric fidelity—crucial under Earth's field NMR conditions where both signal amplitude and spatial resolution are inherently limited.

Table 3.1 Typical coil parameters of the EFNMR system

Coil Parameter	Polarizing Coil	Gradient Coils (pgse, x, y, z)	B_1 Coil
	Value	Value	Value
Avg. coil diameter (mm)	170	105	84
Calc. mag. Field (mT/A)	3.13	N/A	30
Field gradient (mT/m/A)	N/A	2.38, 0.31, 0.28, 0.28	N/A
Avg. Resistance (Ω incl. cable)	2.8	3.1 / 2.0 / 1.5 / 1.5	325
Tuning cap for 2300 Hz (nF)	N/A	N/A	9.7

Unlike conventional high-field NMR systems that employ superconducting magnets to achieve field homogeneity on the order of 1,ppm, Earth's Field NMR (EFNMR) utilizes the naturally uniform geomagnetic field (~50,μT) as its static field (B_0). Although the field strength is several orders of magnitude lower, its macroscopic homogeneity permits the use of larger sample volumes, partially offsetting the inherently low signal arising from weak nuclear polarization.

To enhance initial magnetization, a transient pre-polarization field—typically ~350 times stronger than B_0—is applied using a non-uniform electromagnet. This field is rapidly switched off before FID acquisition begins in the ambient Earth's field.

Since both the magnitude and orientation of the geomagnetic field vary with geographic location (25–65,μT), optimal performance requires site-specific tuning of the receiver coil and precise alignment of the system's B_0 axis with the local geomagnetic vector.

3.1.2 Coil Systems

A dedicated solenoidal coil generates a transient polarization field B_p significantly stronger than the Earth's field (~ 50 μT), reaching up to 18.8 mT at 6.0 A. This field temporarily aligns the sample's nuclear magnetization along the coil's x-axis. After a typical 4–5 s polarization period, the current is adiabatically ramped down, allowing the magnetization to realign with the Earth's field (B_0, aligned with the z-axis).

This pre-polarization increases the spin population difference per the Boltzmann distribution, enhancing net longitudinal magnetization and improving SNR in ultra-low field conditions where intrinsic polarization is otherwise weak.

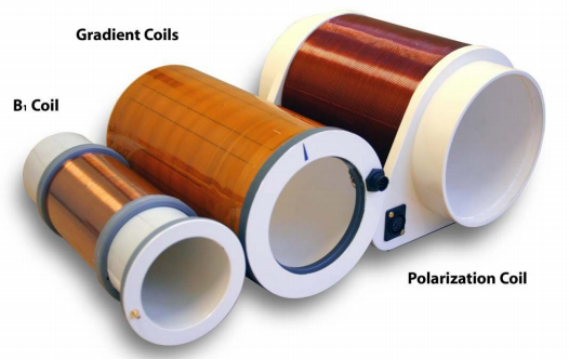

Fig. 3.2 A view of the three EFNMR/MRI coil

Thermal management is essential, as resistive heating scales with current squared. A dissipation limit of $\leq 2\,\mathrm{W}$ and probe temperatures below $40\,^{\circ}\mathrm{C}$ are recommended for operational safety.

Gradient Coil System

The gradient system includes three orthogonal imaging/shimming coils. The gradient coil, aligned along x, provides gradients up to $4.76\,\mathrm{mT/m}$ at $2.0\,\mathrm{A}$ with a per-amp efficiency of $2.38\,\mathrm{mT\cdot m^{-1}\cdot A^{-1}}$, enabling diffusion weighting and spatial encoding while maintaining a low duty cycle ($\sim 2.5\%$) to limit heating.

The imaging and shim coils, implemented as PCB windings, apply z-, y-, and x-axis gradients (~ 55–$63\,\mu\mathrm{T/m}$) for field compensation and encoding at low currents ($\leq 200\,\mathrm{mA}$), ensuring minimal thermal and electrical load.

RF Excitation and Signal Detection

A high-inductance, low-resistance solenoidal B_1 coil, positioned concentrically at the probe center, is used for RF excitation and signal detection at the Larmor frequency (~ 2–$2.5\,\mathrm{kHz}$ for protons under Earth's field).

A tuned 90° RF pulse tips the magnetization into the transverse plane, after which the free induction decay (FID) is detected. The B_1 coil, tuned via an external capacitor, is shielded by shorting the polarization coil during acquisition, enhancing SNR by 15–20× compared to unshielded configurations. Its compact design ensures high sensitivity and spatial localization while minimizing axial field nonuniformity.

3.1.3 EFNMR Spectrometer

Signal acquisition and experimental sequencing are managed via a digital signal processor (DSP) embedded within the EFNMR spectrometer unit. The DSP is controlled by a PC interface running the proprietary *Prospa* software, which handles pulse sequence programming, synchronization, and data retrieval. Communication between the PC and DSP occurs over USB, and once data are collected, the software enables real-time visualization, post-processing, and parameter adjustments.

The system architecture includes direct cable interfaces to the B_1, gradient, and polarization coils, and the entire spectrometer is powered by a 24 V DC source. Figure 3.3 illustrate the connection scheme and the front panel layout of the EFNMR spectrometer, respectively.

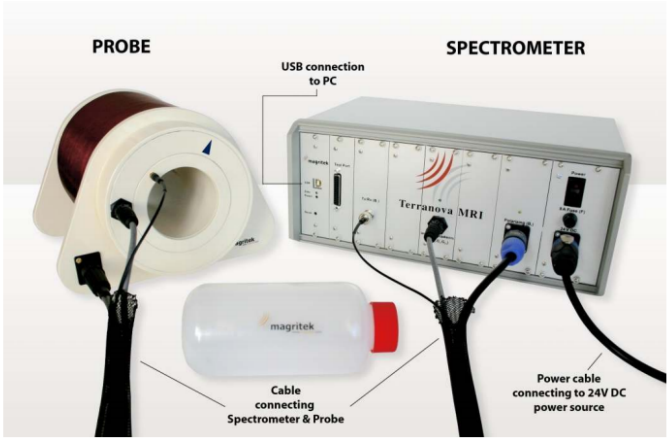

Fig. 3.3 The entire EFNMR system: Spectrometer and Prob

3.2 Choice of Experimental Sample

Water was selected as the experimental sample for ultra-low field MRI due to its optimal physical and practical properties.

Protons in water have a high gyromagnetic ratio ($\gamma = 42.577\,\text{MHz/T}$), enabling higher Larmor frequencies and clear spectral resolution even under the Earth's field:

$$\Delta E = \gamma \hbar B_0.$$

Its high proton density ($\sim 6.7 \times 10^{22}\,\text{protons/cm}^3$) ensures measurable magnetization despite the low polarization under ultra-low field conditions.

Rapid isotropic motion of water molecules averages out dipolar interactions, leading to narrow NMR linewidths and reduced inhomogeneous broadening, which are essential for reliable signal detection under ultra-low field conditions. Moreover, water is stable, non-toxic, and well-characterized, facilitating calibration and theoretical modeling. Its physical properties also approximate those of biological tissues, making water an ideal medium for transitioning from phantom studies to real-world applications in earth's field MRI.

3.3 MRI Theory

Magnetic Resonance Imaging (MRI) originates from the fundamental physics of Nuclear Magnetic Resonance (NMR), a phenomenon first reported independently by Bloch and Purcell in 1946. NMR describes the interaction between nuclear magnetic moments and an external magnetic field. In a typical case such as hydrogen (^{1}H), the nuclear spins tend to align either parallel or antiparallel to a static magnetic field B_0, resulting in a net magnetization vector $\mathbf{M}_0$ aligned with the field.

3.3.1 Larmor Frequency and Spin Precession

When placed in the magnetic field B_0, the nuclear magnetic moments precess about the field direction at a frequency known as the **Larmor frequency**, given by:

$$\omega_0 = \gamma B_0 \tag{3.1}$$

where γ is the gyromagnetic ratio of the nucleus. The Larmor frequency represents the fundamental resonance condition for nuclear spins in MRI. For hydrogen in Earth's magnetic field ($B_0 \approx 56\,\mu$T), $\omega_0 \approx 2.4$ kHz, which determines both the excitation frequency and the phase evolution of the transverse magnetization.

3.3.2 Free Induction Decay and Bloch Dynamics

At thermal equilibrium, the net magnetization $\mathbf{M}_0$ aligns with the static field B_0. An RF pulse at the Larmor frequency tips $\mathbf{M}_0$ into the transverse plane, initiating **free precession** and generating an oscillating signal known as the **Free Induction Decay (FID)**.

The magnetization dynamics follow the **Bloch equations**:

$$\begin{aligned}
\frac{dM_x}{dt} &= \gamma(\mathbf{M}\times\mathbf{B})_x - \frac{M_x}{T_2},\\
\frac{dM_y}{dt} &= \gamma(\mathbf{M}\times\mathbf{B})_y - \frac{M_y}{T_2},\\
\frac{dM_z}{dt} &= \gamma(\mathbf{M}\times\mathbf{B})_z - \frac{M_z - M_0}{T_1},
\end{aligned}$$

where T_1 and T_2 are the longitudinal and transverse relaxation times.

The FID signal is expressed as:

$$s(t) = M_0 e^{-t/T_2} e^{i\omega_0 t},$$

representing a decaying sinusoid at the Larmor frequency with an envelope determined by T_2.

3.3.3 Signal Modeling in Earth's Field MRI

In Earth's Field MRI (EF-MRI), a transient orthogonal polarization field B_p is applied before acquisition to enhance magnetization. After a polarization period τ_p, B_p is removed, allowing spins to precess under the Earth's field B_0.

The detected FID signal can be modeled as:

$$E(t) = C \cdot M_0[1 - e^{-\tau_p/T_1}]e^{-t/T_2^*}\cos(\gamma B_0 t)\sin(\theta_{\text{tip}}),$$

where C is a system constant and θ_{tip} is the flip angle.

A simplified expression under EF-MRI conditions is:

$$s(t) = \gamma^2 B_0 \eta V t_p T_2^* \sin(\alpha) M_{\text{eq}} e^{-t/T_2^*},$$

where η is the polarization efficiency, α the flip angle, and M_{eq} the equilibrium magnetization during polarization.

3.3.4 3D k-space Formalism

MRI signal acquisition fundamentally relies on spatial encoding through gradient fields, resulting in sampling of the reciprocal space known as k-space. Consider a small voxel (Fig. 3.4) at position $\mathbf{r} = (x, y, z)$ with spin density $\rho(\mathbf{r})$ and volume element dV_s. During a

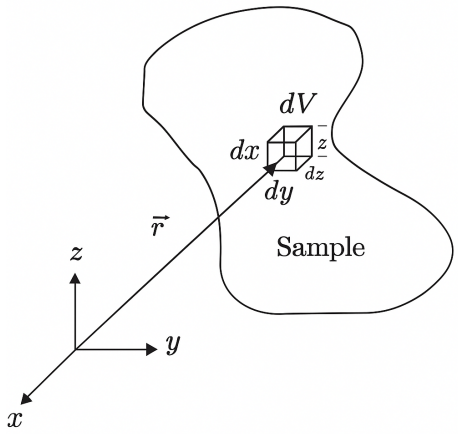

Fig. 3.4 Small voxel within the sample

pulse-and-collect sequence, gradients applied for phase encoding and readout induce a position-dependent phase shift in the acquired signal.

The spatial frequency is defined as:

$$\mathbf{k}(t) = \frac{\gamma}{2\pi} \int_0^t \mathbf{G}(\tau) d\tau,$$

where γ is the gyromagnetic ratio, and $\mathbf{G}(t)$ is the applied gradient vector.

The resulting signal from the voxel can be expressed as:

$$s(t) = \rho(\mathbf{r})\, e^{i2\pi \mathbf{k}(t)\cdot\mathbf{r}}. \tag{3.2}$$

Integrating over the entire sample volume yields the total acquired signal:

$$E(\mathbf{k}) = \iiint \rho(\mathbf{r})\, e^{i2\pi \mathbf{k}\cdot\mathbf{r}} d\mathbf{r}, \tag{3.3}$$

revealing that the MRI signal in k-space is the 3D Fourier transform of the spin density $\rho(\mathbf{r})$.

3.3.5 Fourier Transform and MRI Image Formation

The inverse Fourier Transform is employed to reconstruct spatial images from k-space data:

$$\rho(\mathbf{r}) = \iiint E(\mathbf{k})\, e^{-i2\pi \mathbf{k}\cdot\mathbf{r}} d\mathbf{k}. \tag{3.4}$$

This demonstrates that MRI is inherently a Fourier imaging modality, where gradient fields encode spatial frequencies into the acquired signal, enabling spatial localization upon reconstruction.

Both Gradient Echo (GRE) and Spin Echo (SE) sequences utilize this Fourier-based k-space acquisition but differ in phase correction and contrast:

- **Gradient Echo (GRE)**: Uses a single RF excitation followed by gradient reversal to rephase spins, allowing rapid acquisition and T_2^*-weighted imaging, but is more sensitive to field inhomogeneities.
- **Spin Echo (SE)**: Utilizes a 90° excitation pulse followed by a 180° refocusing pulse, compensating for field inhomogeneities and providing true T_2-weighted images.

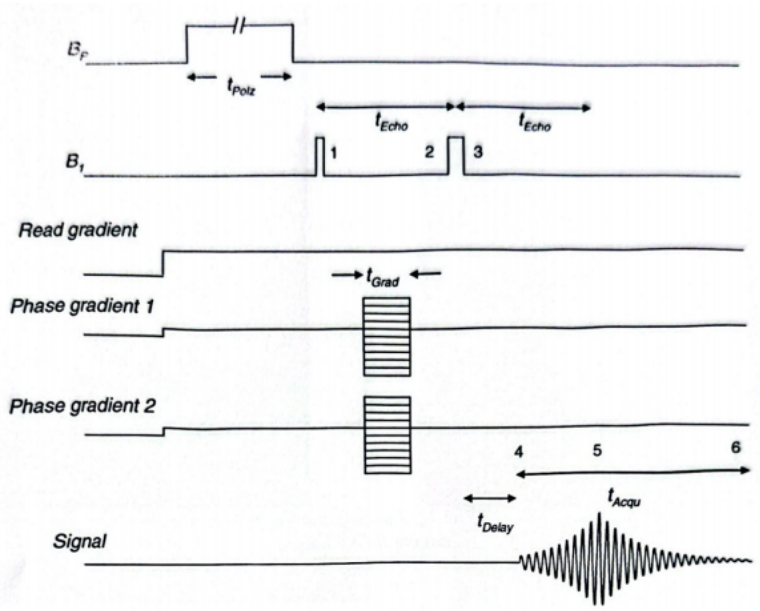

Fig. 3.5 Spin Echo Pulse Sequence

These sequences illustrate practical implementations of Fourier-based spatial encoding in MRI, underlining the central role of k-space sampling and inverse Fourier reconstruction in image formation.

3.4 Quantitative Evaluation Metrics for Denoising Effect

To quantitatively assess the denoising performance of the EF-MRI reconstruction pipeline, we employed multiple image quality metrics, including Signal-to-Noise Ratio (SNR), Root

Mean Square (RMS) noise, Mean Squared Error (MSE), Peak SNR (PSNR), and Structural Similarity Index (SSIM). Together, these metrics capture signal fidelity, noise suppression, and perceptual image quality from complementary perspectives.

SSIM decomposes image similarity into three components: luminance (l), contrast (c), and structure (s), calculated as follows:

$$l(X,Y) = \frac{2\mu_X\mu_Y + C_1}{\mu_X^2 + \mu_Y^2 + C_1} \tag{3.5}$$

$$c(X,Y) = \frac{2\sigma_X\sigma_Y + C_2}{\sigma_X^2 + \sigma_Y^2 + C_2} \tag{3.6}$$

$$s(X,Y) = \frac{\sigma_{XY} + C_3}{\sigma_X\sigma_Y + C_3} \tag{3.7}$$

Their values are computed by:

$$\mu_X = \frac{1}{MN}\sum_{i=1}^{M}\sum_{j=1}^{N} X(i,j) \tag{3.8}$$

$$\mu_Y = \frac{1}{MN}\sum_{i=1}^{M}\sum_{j=1}^{N} Y(i,j) \tag{3.9}$$

$$\sigma_X^2 = \frac{1}{MN-1}\sum_{i=1}^{M}\sum_{j=1}^{N} (X(i,j) - \mu_X)^2 \tag{3.10}$$

$$\sigma_Y^2 = \frac{1}{MN-1}\sum_{i=1}^{M}\sum_{j=1}^{N} (Y(i,j) - \mu_Y)^2 \tag{3.11}$$

$$\sigma_{XY} = \frac{1}{MN-1}\sum_{i=1}^{M}\sum_{j=1}^{N} (X(i,j) - \mu_X)(Y(i,j) - \mu_Y) \tag{3.12}$$

Then, the final SSIM index is given by:

$$\mathrm{SSIM}(X,Y) = l(X,Y)\cdot c(X,Y)\cdot s(X,Y) \tag{3.13}$$

CHAPTER 4

Experimental Implementation and Results

4.1 System Setup and Calibration

4.1.1 Environmental Setup and Probe Orientation

The apparatus was installed in a research facility located in Dublin city centre, an urban environment characterized by substantial magnetic and electromagnetic activity. This setup highlights the practical challenge of operating Earth's Field NMR in magnetically noisy metropolitan environments.

The EFNMR probe was mounted on a non-magnetic support—such as a wooden or plastic stand—positioned approximately 1 meter above ground level. All auxiliary components, including the power supply and cables, were positioned at maximal distance from the probe to minimize electromagnetic cross-talk.

A magnetic compass was used to determine the North–South (N–S) geomagnetic axis. The longitudinal axis (x-axis) of the EFNMR probe was then carefully aligned orthogonally to this N–S vector. This ensures optimal coupling with the Earth's field vector B_0, which is required for maximizing signal amplitude.

With the MonitorNoise macro executed via the spectrometer control software, the probe was moved incrementally throughout the room. At each spatial position, the noise amplitude was recorded while maintaining the orthogonal N–S alignment. The final probe location was selected based on the global minimum of this noise map.

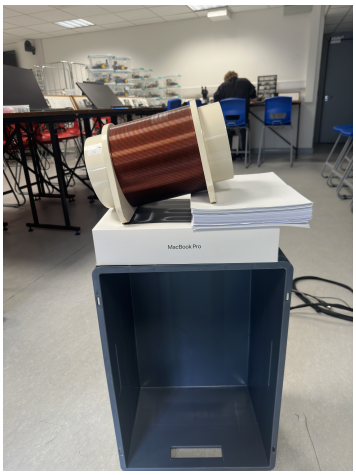

(a) Experiment environment

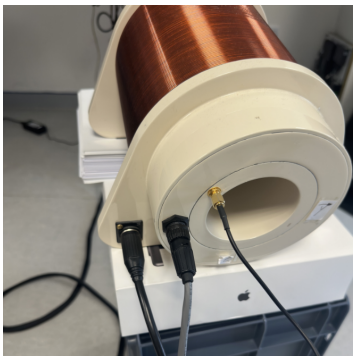

(b) Cable and power connections

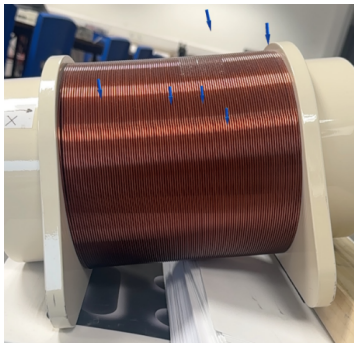

(c) Earth's field vector alignment

Fig. 4.1 System setup and alignment before EF-MRI initialization: (a) physical environment, (b) cabling and connections, (c) orientation of Earth's magnetic field.

Once the optimal spatial coordinates were determined, the probe was fixed in place. A subsequent AutoShim macro was then run to compensate for residual magnetic field inhomogeneities, particularly those induced by surrounding materials or ambient disturbances.

4.1.2 Resonance Verification Based on Measured Geomagnetic Field

To validate the resonance condition and ensure correct system calibration, a verification experiment was performed using a known estimate of the local geomagnetic field in central Dublin. The ambient magnetic field strength was first measured using a mobile phone magnetometer, yielding an approximate value of $B_0 \approx 45\,\mu\text{T}$.

Given this value, the expected proton Larmor frequency can be calculated using:

$$f_0 = \frac{\gamma B_0}{2\pi} \approx \frac{2.675 \times 10^8 \cdot 45 \times 10^{-6}}{2\pi} \approx 1.91\,\text{kHz} \tag{4.1}$$

where $\gamma = 2.675 \times 10^8\,\text{rad} \cdot \text{s}^{-1} \cdot \text{T}^{-1}$ is the gyromagnetic ratio for the proton.

To verify this prediction, the spectrometer's `AutoTune` function was used to perform a frequency sweep across the RF resonance range. A prominent peak was experimentally observed near 1.91 kHz, matching the theoretical value and confirming proper tuning of the B_1 coil circuit.

This successful match validates the magnetic alignment of the system and enables reliable acquisition of echo-based imaging sequences. The full list of initialization parameters is shown in Table 4.1.

Table 4.1 Suggested initial parameter values

Parameter	**Value**	**Parameter**	**Value**
Capacitance	Run AutoTune	B_1 frequency (Hz)	Run AutoTune
B_1 pulse length (ms)	1.5	Polarization time (ms)	4000
Polarization current (A)	6	Transmit gain	2.5
Receive gain	2	Number of points	16,384
Acquisition time (s)	1	90° acquisition delay (ms)	25
Display range (Hz)	400	Number of scans	1

4.1.3 Shim Field Calibration via AutoShim

Figure 4.2 presents a comparison between raw Free Induction Decay (FID) signals and their corresponding spectra acquired before and after the AutoShim process.

In Subfigures (b) and (d), the pre-shim FID shows a rapidly damped signal with significant oscillations and noise, indicating magnetic field inhomogeneity. Its spectrum reveals a broadened resonance peak and relatively low peak amplitude, resulting in reduced signal clarity and poor spectral resolution.

In contrast, Subfigures (a) and (c), illustrates the FID and FFT spectrum after applying shim corrections. The post-shim FID exhibits a more slowly decaying envelope and improved symmetry, suggesting better field homogeneity. The frequency domain spectrum shows a much sharper peak with higher amplitude, demonstrating a notable enhancement in signal-to-noise ratio (SNR) and effective line narrowing.

Figure 4.3 shows the output spectrum generated during the AutoShim routine, which is based on the Fourier Transform of the Free Induction Decay (FID) acquired immediately after each shim iteration. This spectrum reflects the direct response of the system to field homogeneity changes.

Figure 4.4, in contrast, presents the spectrum obtained after applying the finalized shim values during a Spin Echo acquisition. Here, the echo formation mitigates dephasing effects caused by minor field inhomogeneities. The resulting spectrum exhibits a noticeably sharper resonance peak, narrower linewidth, and significantly enhanced signal-to-noise ratio (SNR), validating the effectiveness of the AutoShim-determined shim settings.

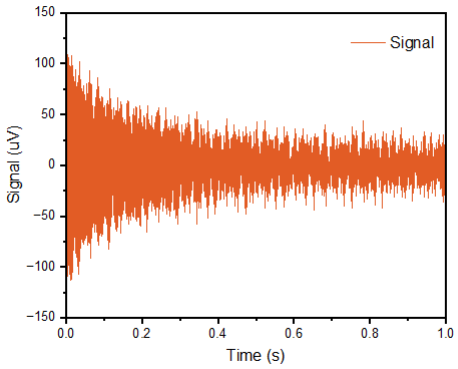

(a) Shimmed: Time Domain

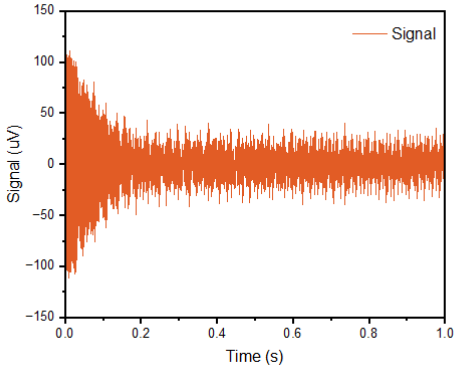

(b) Unshimmed: Time Domain

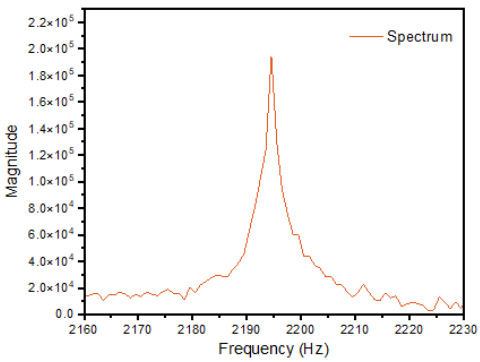

(c) Shimmed: Frequency Domain

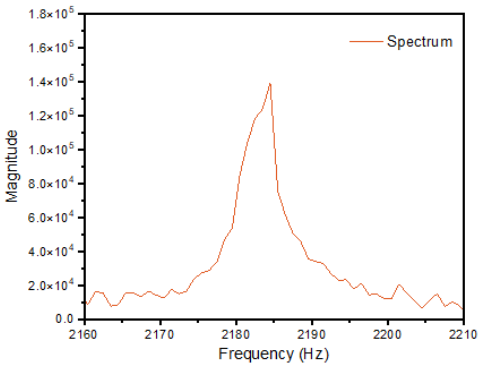

(d) Unshimmed: Frequency Domain

Fig. 4.2 Comparison of the FID signals and spectra before and after shimming.

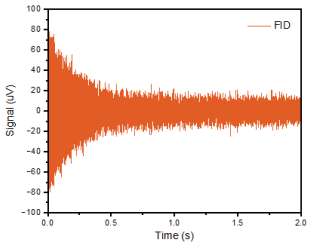

(a) Raw FID signal

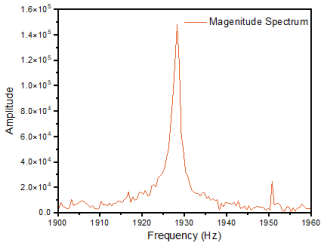

(b) Magnitude spectrum

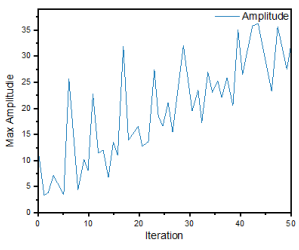

(c) Optimization curve

Fig. 4.3 FID-based AutoShim results: (a) raw FID signal, (b) magnitude spectrum, and (c) optimization curve showing peak amplitude across iterations.

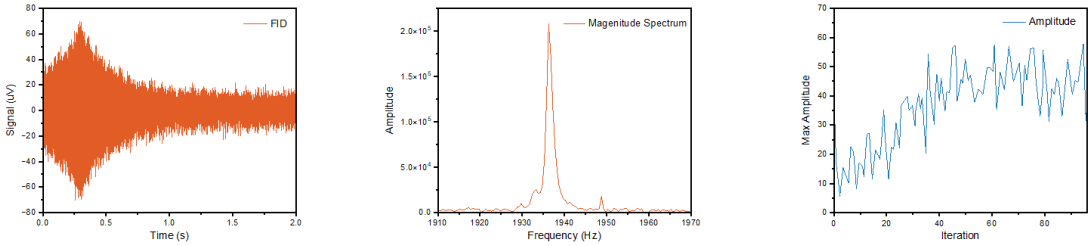

(a) Raw FID after echo signal (b) Magenitude Spectrum (c) Optimization curve

Fig. 4.4 Spin Echo-based AutoShim: (a) raw FID signal, (b) magnitude spectrum, and (c) optimization curve showing peak amplitude across iterations.

The distinction between the two figures highlights the difference in signal characteristics between simple FID-based optimization and echo-based acquisition sequences. This discrepancy reinforces the need to calibrate and validate shim results under the actual imaging sequence of interest.

Together, these validation steps conclude the system setup phase and establish a reliable baseline for the execution of the subsequent NMR imaging protocols.

4.1.4 RF Pulse Calibration: B1 Duration Optimization

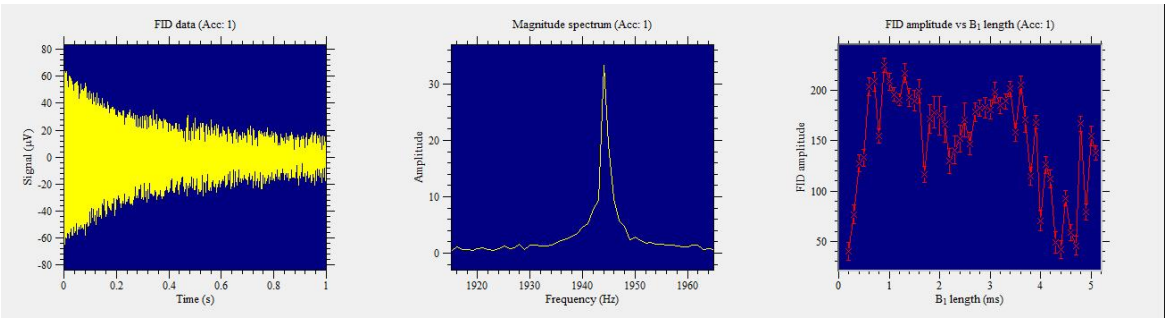

Fig. 4.5 B_1Duration optimization results. (a) Raw FID signal; (b) frequency spectrum showing resonance at 1942 Hz; (c) FID amplitude versus B_1 pulse duration.

To achieve efficient spin excitation, a B1 Duration experiment was performed following field shimming to determine optimal 90° and 180° RF pulse durations. The B_1 pulse width was incrementally varied from 0.227 ms to 3.5 ms in 15 steps, and the FID amplitude at each step was computed by integrating a narrow frequency band (±5–10 Hz around resonance).

As shown in Figure 4.5, the amplitude-duration plot exhibits a sinusoidal profile, where the first peak and subsequent minimum correspond to the 90° and 180° conditions.

Subfigure (a) shows the raw FID signal, (b) the frequency-domain spectrum centered at 1942 Hz, and (c) the fitted nutation curve used to extract the flip angles.

Repeated measurements showed stable 90° and 180° durations around 1.0–1.1 ms and 2.0–2.2 ms, respectively. A consistent dip near 0.75 ms was observed across multiple datasets, likely due to transient coil ring-down or amplifier instability.

4.2 EF-NMR Experimental Implementation and Analysis

Following the completion of B_1 calibration and shim field optimization, a series of foundational NMR measurements were conducted to evaluate the quality and stability of Free Induction Decay (FID) signals under current system conditions (Fig.4.6) . These measurements form the experimental basis for subsequent imaging sequences.

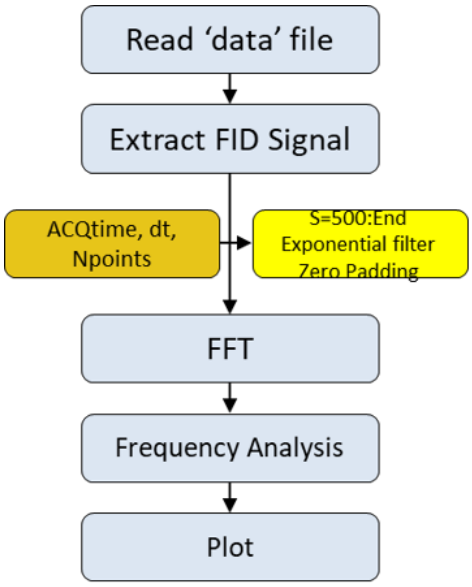

Fig. 4.6 Signal processing pipeline for EFNMR FID data.

4.2.1 FID Signals Acquisition and Comparison

Figure 4.8 presents in the time domain, the orange curve represents the FID response from the sample containing water, characterized by coherent oscillations and exponential decay. In contrast, the blue curve (acquired without the sample) shows low-amplitude stochastic fluctuations consistent with thermal or electronic noise.

The corresponding frequency-domain spectra further highlight this difference. The loaded condition exhibits a distinct resonance peak near 2193,Hz, consistent with the

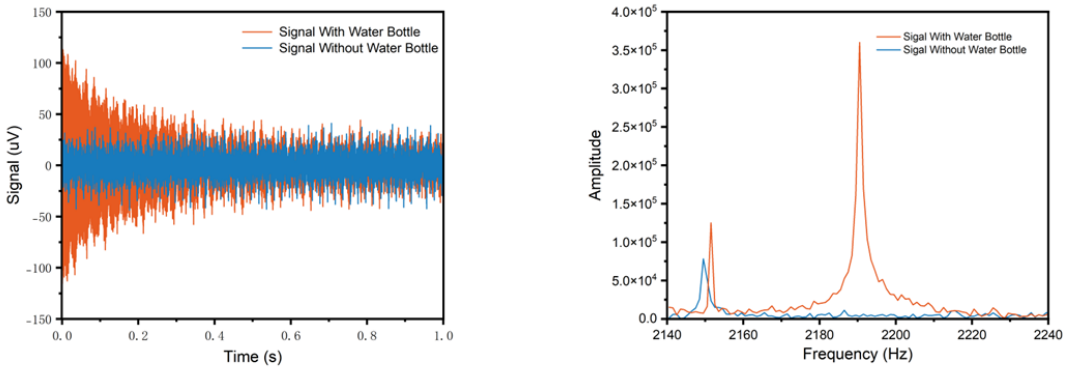

(a) FID signals with and without water bottle.

(b) FFT spectra with and without water bottle.

Fig. 4.7 Comparison of EF-MRI signals

hydrogen Larmor frequency at the Earth's magnetic field strength in Dublin. No discernible peak is observed in the unloaded spectrum, confirming the absence of detectable nuclear spin response.

4.2.2 Temporal Signal Enhancement via Exponential Weighting

To emphasize the high-SNR portion of the FID and mitigate the influence of late-time noise, an exponential weighting filter was applied according to the formulation:

$$\text{Filtered Signal}(t) = \text{Signal}(t) \cdot e^{-t/\tau}$$

with a decay constant of $\tau = 0.15\,\text{s}$.

The decay constant was chosen because the majority of the coherent signal energy in the FID is concentrated within the first 100–200 milliseconds. This initial segment contains the highest signal amplitude and is least affected by thermal noise, baseline drift, and dephasing artifacts. By applying an exponential filter with $\tau = 0.15\,\text{s}$, the time-domain signal is weighted to emphasize this early high-SNR region, while gradually attenuating the later-time noise-dominated tail. This approach enhances spectral clarity without severely distorting the main resonance peak.

This operation serves as a temporal windowing function that selectively attenuates low-coherence signal components occurring at longer acquisition times. As illustrated in the left panel of Figure 4.8, the application of the exponential filter suppresses the noisy tail of the FID signal while preserving the initial high-amplitude portion, resulting in a smoother and more localized signal envelope.

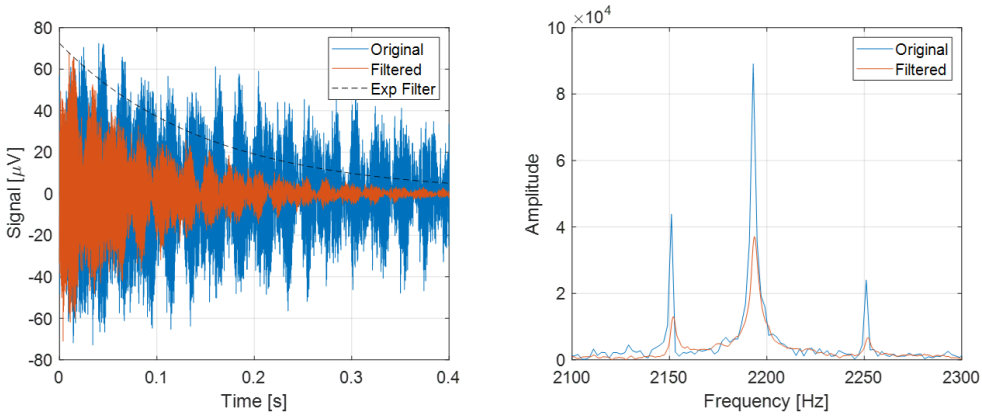

Fig. 4.8 Time and frequency domain effects of exponential filtering on an FID signal. *Left*: The original FID signal (blue) is modulated by an exponential window with a decay constant of $\tau = 0.15\,\text{s}$, producing the filtered signal (orange). *Right*: Corresponding frequency-domain spectra before and after filtering. The central peak represents the MRI signal, while the symmetric side peaks correspond to 50 Hz harmonic noise signals arising from power-line interference.

In the frequency domain (right panel), this filtering operation significantly improves spectral clarity: the main resonance peak remains sharp and well-defined, while the 50 Hz harmonic noise, commonly attributed to power-line interference, is effectively suppressed. Additionally, side-lobe artifacts are reduced, yielding a cleaner spectral baseline and enhanced harmonic separation.

4.2.3 Assessment of Signal Reproducibility and Frequency Stability

In light of the known susceptibility of Earth's Field MRI (EF-MRI) to environmental noise and frequency drift, especially in urban settings, we evaluated the stability of optimized FID signals across 100 consecutive acquisitions. All acquisitions were performed under identical shim, polarization, and acquisition parameters.

The results are summarized in Figure 4.9. It illustrates the resonance frequency distribution across recordings, with the mean frequency centered at 2193.62 Hz—closely aligned with the theoretical Larmor frequency in Dublin (2193.87 Hz under a geomagnetic field of 51 μT).

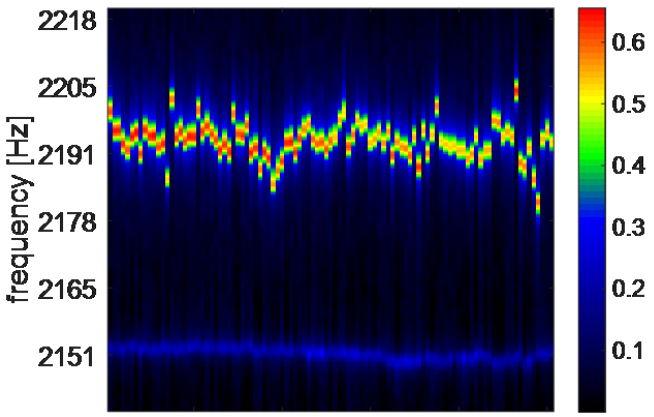

Fig. 4.9 Stability analysis of FID signals across 100 acquisitions [7]. This result also reflects the potential of EF-MRI systems to function as magnetometers, as previously highlighted in the literature review.

4.2.4 Temporal Stability Evaluation

To quantitatively assess the temporal stability of the EFNMR acquisition system, we evaluated the signal-to-noise ratio (SNR) and root-mean-square (RMS) noise across 100 consecutive Free Induction Decay (FID) measurements.

The SNR, expressed in decibels (dB), was calculated using a standard logarithmic ratio between the peak signal amplitude and the baseline noise standard deviation. RMS noise was similarly quantified based on the statistical variance of noise-only regions. As

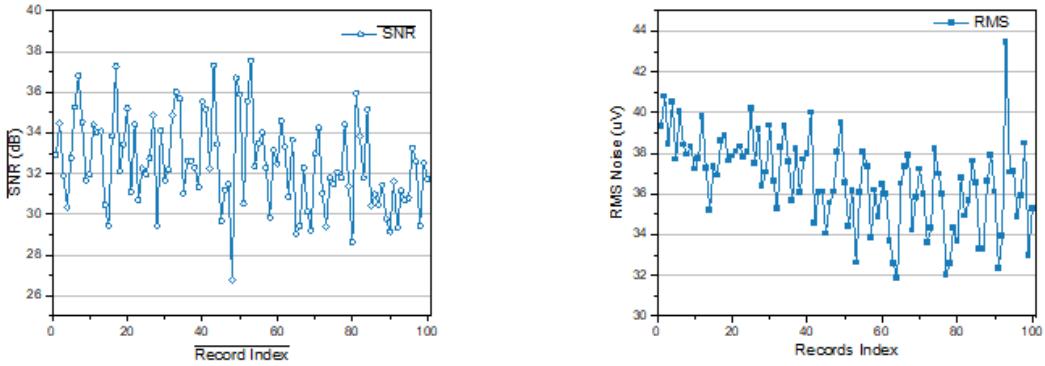

(a) SNR across 100 records.

(b) RMS noise across 100 records.

Fig. 4.10 Temporal stability evaluation of the EFNMR system showing SNR (left) and RMS noise (right) over 100 consecutive records.

illustrated in Figure. 4.10a, the SNR values fluctuate between 27 dB and 38 dB, with a

median value around 32 dB. This level of variability highlights the system's susceptibility to ambient magnetic disturbances, thermal drift, and inherent instabilities in the excitation and detection hardware.

Figure. 4.10b shows the corresponding RMS noise amplitude, which ranges from 32 μV to 42 μV. The occurrence of intermittent high-amplitude outliers suggests the influence of transient environmental disturbances, such as electromagnetic interference or mechanical vibrations. These findings underscore the importance of implementing robust environmental controls—such as magnetic shielding, thermal stabilization, and mechanical isolation—to ensure consistent and reliable signal acquisition in ultra-low-field nuclear magnetic resonance (ULF-NMR) systems.

4.3 1D EF-MRI: Experimental Implementation and Analysis

4.3.1 1D Imaging Signal Processing Pipeline

In 1D earth's field MRI systems, signal acquisition is fundamentally conducted in the time domain, where the detected Free Induction Decay (FID) comprises oscillating voltage responses induced by precessing nuclear magnetization. However, to extract spatial information from these time-domain signals, it is essential to perform a transformation into the frequency domain. This is most effectively achieved through complex signal representation and subsequent Fourier analysis.

As illustrated in Figure 4.11, the FID signal is initially extracted from the acquired `.data` file and converted into a complex-valued function:

$$s(t) = Ae^{i(\omega t+\phi)} \tag{4.2}$$

This representation captures both amplitude and phase evolution, a critical requirement for encoding directional information intrinsic to Magnetic Resonance Imaging. Complex exponentials naturally accommodate the phase rotation resulting from nuclear spin precession under the Earth's magnetic field B_0, providing a mathematically tractable form for frequency-based reconstruction.

To enhance the fidelity of spectral reconstruction, a series of preprocessing steps are applied.First, an exponential decay window $w(t)$ is multiplied with the raw complex FID

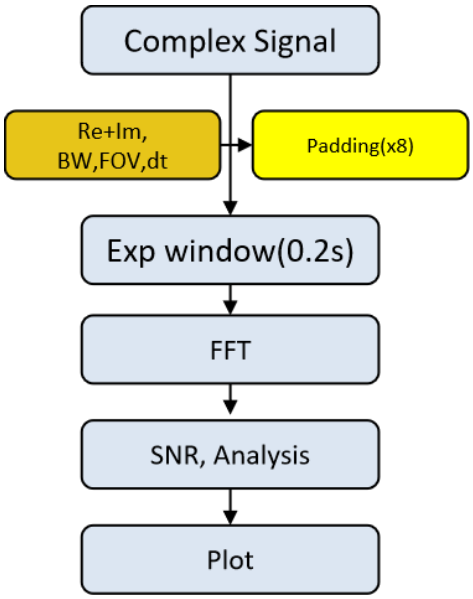

Fig. 4.11 Signal processing pipeline for 1D imaging: from raw FID extraction to frequency-domain spatial mapping.

signal, attenuating incoherent components and improving spectral sharpness:

$$s_{\text{filtered}}(t) = s(t) \cdot w(t), \quad w(t) = \begin{cases} 1, & t < t_0 \\ e^{-k(t-t_0)}, & t \geq t_0 \end{cases} \tag{4.3}$$

Here, t_0 marks the onset of the decay window, typically selected around 0.2 seconds to preserve high-SNR signal components.

Zero-padding is then applied to the filtered signal, extending the time-domain vector length without altering its frequency content. This technique effectively increases the frequency resolution of the subsequent Fourier Transform (FFT), enabling more precise spatial localization of spectral peaks.

Following these operations, the FFT is performed to yield the spatial-domain projection of spin density along the readout axis.

In Earth's Field MRI experiments, minor environmental variations and instrumental instabilities can induce frequency drifts during acquisition, as the Larmor frequency is directly determined by the Earth's field(Fig.4.12). These drifts manifest as positional shifts in the resulting one-dimensional images, degrading spatial accuracy and consistency. To address this, an automatic frequency correction strategy leveraging spectral peak localization is applied prior to reconstruction. This approach accommodates both single-

peak and dual-peak scenarios, ensuring robust alignment of spectral peaks and preserving the true spatial positions within the sample.

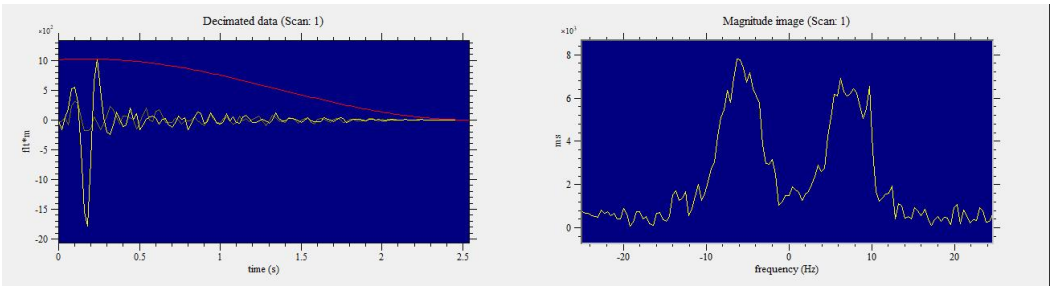

(a) Scan 1

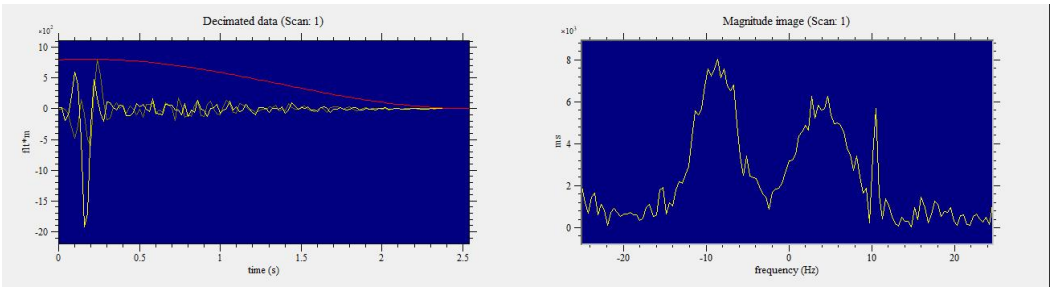

(b) Scan 2

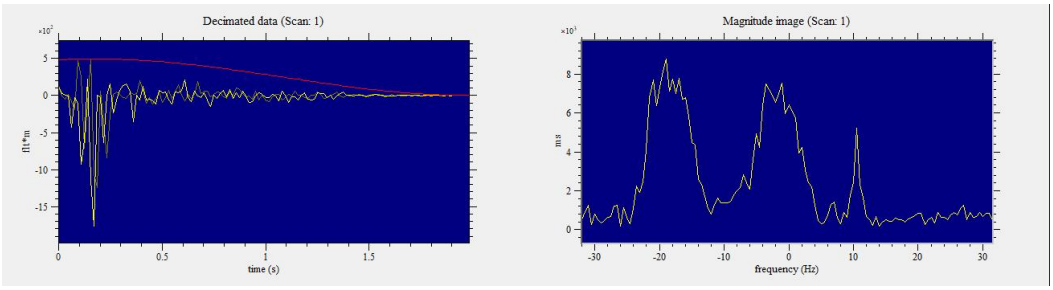

(c) Scan 3

Fig. 4.12 Repeated 1D imaging results along the Z-axis for a two-vial sample. In each subfigure, the left panel shows the filtered FID signal in the time domain, and the right panel displays its corresponding frequency-domain magnitude spectrum. These results demonstrate noticeable frequency drifts across repeated acquisitions, underscoring the necessity of auto frequency correction in ultra-low field MRI signal processing.

Single-Peak Case For spectra exhibiting a single dominant resonance peak, the correction procedure begins by identifying the frequency f_{peak} corresponding to the spectral maximum. The offset from the nominal B_1 frequency f_{B1} is then computed as:

$$\Delta f = f_{\text{peak}} - f_{B1}$$

This offset is applied as a complex exponential modulation to the original time-domain signal $s(t)$, effectively realigning the spectrum:

$$s_{\text{corrected}}(t) = s(t) \cdot e^{-i2\pi\Delta f t}$$

Dual-Peak Case In spectra containing two resonance peaks (e.g., due to symmetrical compartments in the phantom), we assume approximate spectral symmetry. The two dominant peaks at f_1 and f_2 are detected, and their midpoint is computed as:

$$f_{\text{center}} = \frac{f_1 + f_2}{2}$$

The frequency shift $\Delta f = f_{\text{center}} - f_{\text{B1}}$ is then applied to the time-domain signal in the same manner.

Application This frequency correction method was consistently applied across all datasets and was also integrated into the 2D filtered backprojection (FBP) reconstruction pipeline (Fig.4.13). By aligning spectra prior to Fourier transformation, the correction significantly improved spatial resolution and spectral sharpness in the reconstructed images.

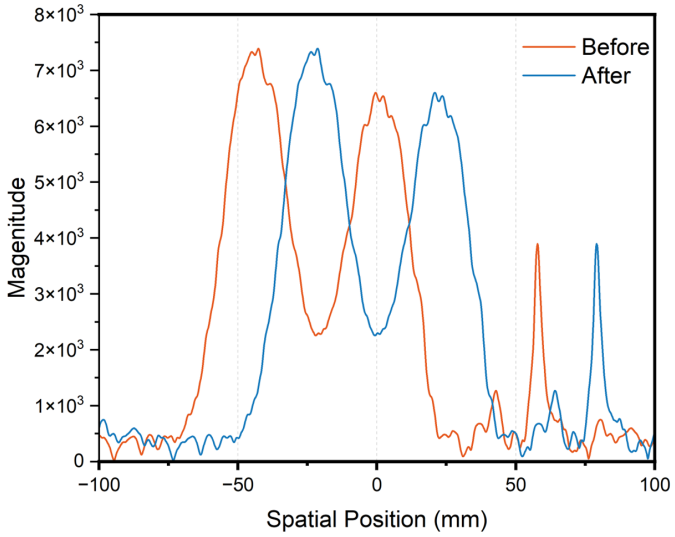

Fig. 4.13 Comparison of original and frequency-corrected FFT spectrum. The correction aligns both resonance peaks symmetrically around the target center frequency (Orange).

4.3.2 Analysis of Experimental Data and Results for Two Sample Types

1D Imaging of a Two-Vial Water Phantom

In this section, we present the 1D Spin Echo imaging experiment conducted using the air-filled vials phantom. The photographs in Fig. 4.14c illustrate the phantom from the X-Y, rotated X-Y, and Y-Z perspectives, providing clear reference views for alignment and reconstruction validation during EF-MRI experiments. These visual references ensure accurate positioning and consistent experimental conditions across repeated measurements.

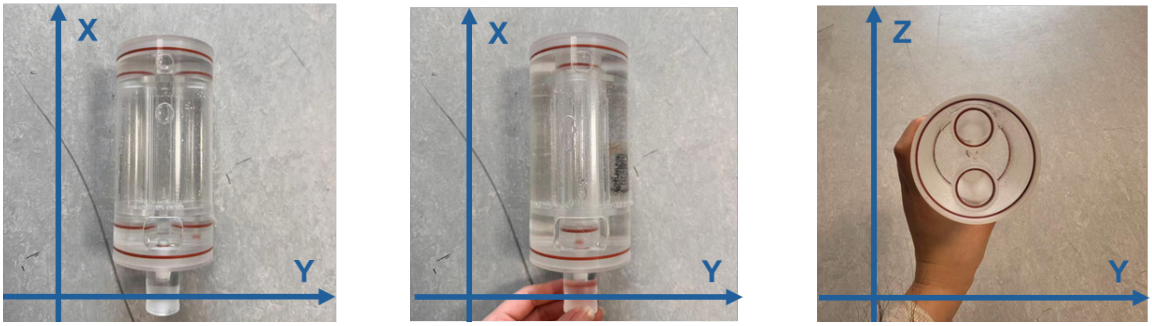

(a) $X-Y$ view. (b) Rotated $X-Y$ view. (c) $Y-Z$ view.

Fig. 4.14 Photographs of the air-filled vials phantom used for EF-MRI experiments, illustrating the $X-Y$, rotated $X-Y$, and $Y-Z$ views for reference during reconstruction and alignment.

Table 4.2 summarizes the key experimental parameters for the Spin Echo 1D imaging acquisition. These settings were determined within the system's experimental workflow to achieve the best performance, balancing signal-to-noise ratio (SNR), acquisition time, and spatial resolution while maintaining consistency with prior EF-MRI measurement protocols.

Fig. 4.15 shows the original complex FID signal acquired from the two-vial phantom along the X direction, demonstrating that the majority of meaningful signal content is confined to the initial 0.2 s following excitation, beyond which the signal amplitude diminishes rapidly and becomes predominantly noise-dominated. These later low-amplitude oscillations contribute negligible spatial information while introducing additional noise into the subsequent spectral analysis. The Fourier transform of this unwindowed FID signal, also shown in Fig. 4.15, reveals a pronounced peak near 1960 Hz, attributed to environmental or system-related interference, which further degrades the spectral quality and reduces the interpretability of the spectrum for accurate spatial localization.

Table 4.2 Experimental parameters for the Spin Echo 1D Imaging experiment.

Parameter	Value
Polarization current (A)	7
Capacitance (pF)	13.35
90° pulse duration (ms)	1.1
Z shim (a.u.)	−21.18
Y shim (a.u.)	6.05
X shim (a.u.)	−1.21
Repetition time, TR (s)	8
Bandwidth (Hz)	32
Echo time, TE (ms)	200
Gradient duration (ms)	50
B1 frequency (Hz)	1940
FOV (mm)	200
Orientation (−)	X,Y,Z
Dimension (−)	1
Position (px)	[863, 495]

To address these limitations and improve spectral sharpness while suppressing noise contributions from later time points, an exponential decay window was applied to the complex FID signal prior to Fourier transformation. The left panel of Fig. 4.16 shows the decay window used in this process, with the red dashed line indicating the onset of decay at 0.2 s, after which the signal is progressively attenuated to reduce the influence of noise-dominated samples. The right panel displays the resulting complex FID signal after windowing, which demonstrates a clear reduction in noise oscillations while preserving the primary features corresponding to the two-vial phantom. This windowing procedure enhances the spectral fidelity by reducing side lobes and improving the signal-to-noise ratio, thereby facilitating more accurate spatial localization and improving the quality of EF-MRI reconstruction.

Following the windowing step, zero-padding was applied to the decay-windowed signal to further enhance the apparent spectral resolution by increasing the density of frequency sampling points in the Fourier domain. Fig. 4.17 presents the decay-windowed and zero-padded complex FID signal alongside its corresponding spectrum. The application of zero-padding does not alter the underlying spectral content but interpolates additional points in the frequency domain, allowing for clearer peak delineation and improved visual discrimination of the spectral features associated with the two-vial phantom. Quantitative analysis shows that the pronounced noise-related peak near 1960 Hz, which had an

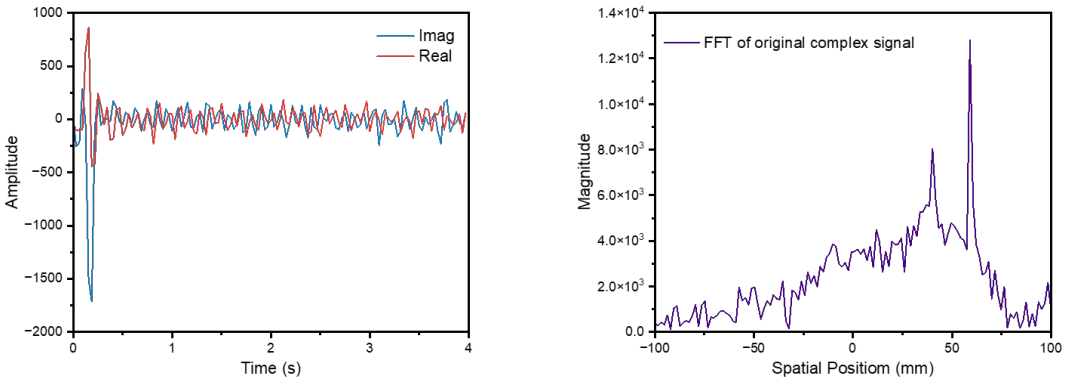

Fig. 4.15 Original FID signal and corresponding FFT for the 1D Spin Echo imaging of the two-vial phantom along the X direction. (Left) The raw time-domain FID signal. (Right) The unfiltered spatial-domain spectrum obtained via FFT.

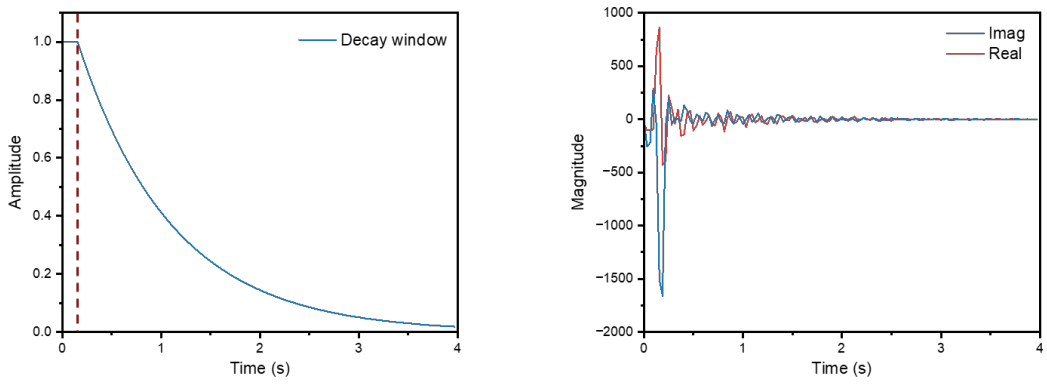

Fig. 4.16 Exponential decay window and its application to the complex FID signal in the 1D Spin Echo imaging experiment. (Left) The applied exponential decay window with the red dashed line indicating the onset of decay. (Right) The resulting complex FID signal after applying the decay window, showing reduced noise oscillations.

amplitude of approximately 12,000 in the unwindowed spectrum, is reduced to around 6,000 following windowing, while the signal-to-noise ratio improves substantially from 8.65 dB to 16.20 dB. These improvements collectively demonstrate the effectiveness of the windowing and zero-padding workflow in enhancing spectral fidelity and resolution, thereby facilitating more accurate EF-MRI image reconstruction and quantitative analysis.

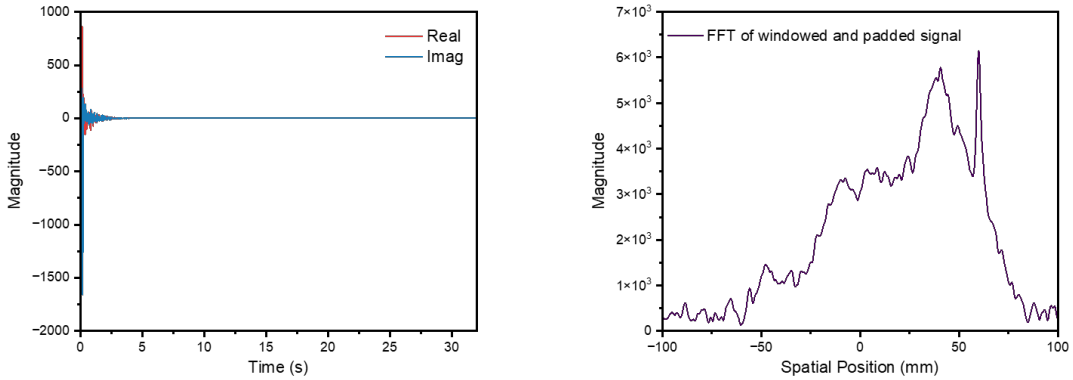

Fig. 4.17 Decay-windowed and zero-padded complex FID signal (left) and its corresponding spatial-domain spectrum (right) for the two-vial phantom along the X direction.

To further facilitate the interpretation of the spatial-domain spectrum and to enable direct spatial localization, a frequency shift was applied to the spectrum to center it within the spatial domain. This step aligns the dominant peaks to the center of the spectrum and allows for a clearer assessment of the physical extent of the phantom along the X axis. Post-processing analysis confirms that the spatial extent of the detected signal along the X direction measures approximately 120 mm, which is consistent with the actual physical length of the two-vial phantom used in the experiment. This consistency between the measured and actual dimensions validates the accuracy of the 1D Spin Echo EF-MRI acquisition and the effectiveness of the signal processing workflow, demonstrating the capability of low-field EF-MRI systems to provide reliable spatial localization when combined with appropriate frequency-domain filtering and alignment strategies.

Fig. 4.19 illustrates the complete signal processing workflow for the 1D Spin Echo EF-MRI experiment along the Y direction, facilitating reproducibility and transparent interpretation of the experimental pipeline.

Panel (a) shows the originally acquired complex free induction decay (FID) signal, with real and imaginary components, following the excitation of the two-vial phantom. It is evident that the primary signal content is concentrated within the initial 0.2 s, while later

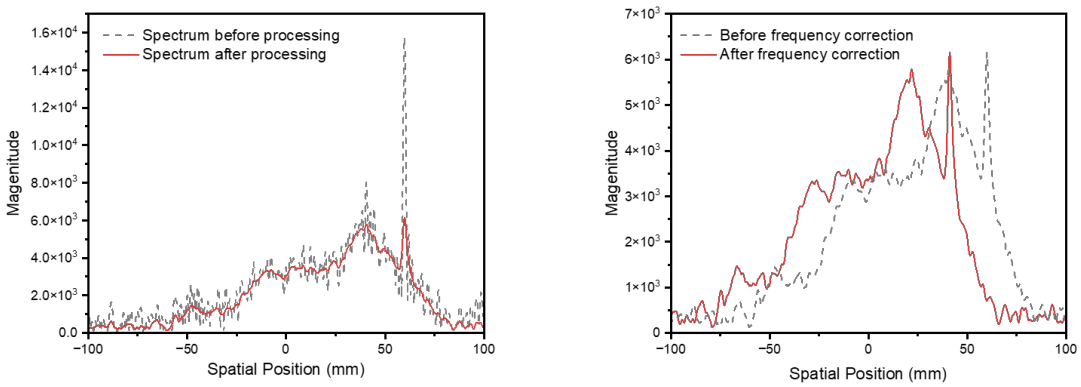

Fig. 4.18 Comparison of spatial-domain spectra before and after processing (left) and with frequency correction applied (right) for the two-vial phantom along the X direction. Processing and frequency correction enhance peak sharpness and alignment, facilitating accurate spatial localization.

time points are dominated by noise and contribute minimally to the spatial information, underscoring the need for time-domain filtering.

To address this, an exponential decay window was applied to the complex FID signal to attenuate noise contributions from later samples, followed by zero-padding to improve frequency resolution during Fourier analysis, as shown in panel (b). This step preserves the signal's primary features while enhancing spectral sharpness by increasing effective sampling density in the frequency domain.

Panel (c) compares the spatial-domain spectra before and after processing, demonstrating that the applied decay windowing and zero-padding substantially reduce the noise floor and sharpen the spectral peaks, which directly correspond to the physical locations of the two vials within the phantom. Quantitative analysis reveals a signal-to-noise ratio (SNR) improvement from 7.53 dB in the raw spectrum to 17.74 dB after processing, confirming the effectiveness of the applied filtering strategy in enhancing spectral fidelity.

Panel (d) shows the physical view of the phantom with the Y direction indicated, providing a spatial reference for interpreting the reconstructed spectra. The alignment between the processed spectral peaks and the known geometry of the phantom validates the accuracy of the low-field EF-MRI acquisition and processing workflow, enabling reliable spatial localization and quantification within the 1D imaging experiment. This systematic approach can be readily replicated in similar EF-MRI studies to improve spectral quality while maintaining consistency in experimental analysis pipelines.

Figure 4.20 presents the 1D spatial projection after a 90° rotation of the phantom. The signal-to-noise ratio (SNR) improves from 7.51 dB to 14.66 dB.

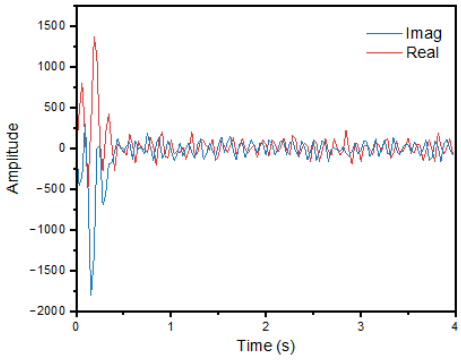

(a) Original complex FID signal along the Y direction.

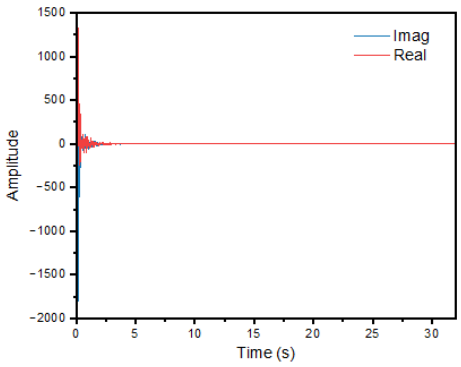

(b) Complex FID signal after decay windowing and zero-padding.

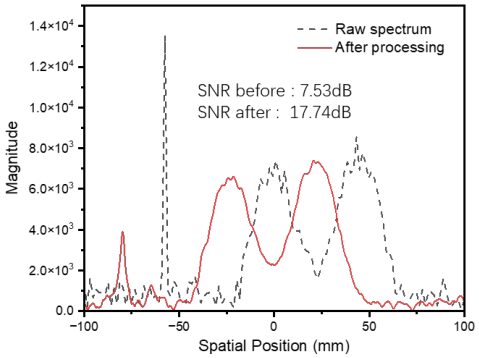

(c) Comparison of FFT before and after processing.

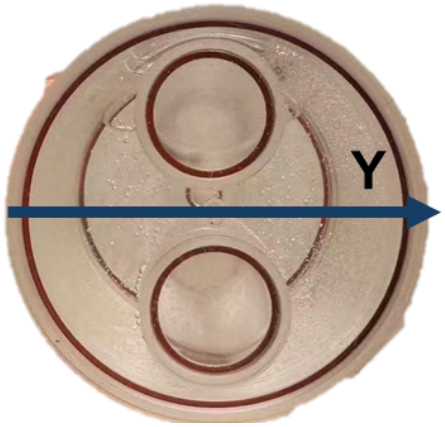

(d) Physical view of the phantom for reference.

Fig. 4.19 Signal processing workflow for 1D Spin Echo EF-MRI along the Y direction, showing raw and processed complex signals, FFT comparison, and physical phantom orientation for reference.

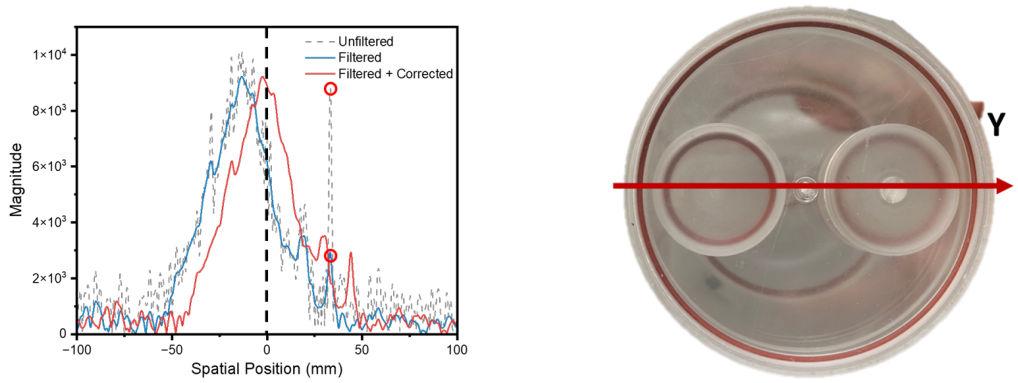

(a) Processed 1D image (Y)

(b) Physical orientation.

Fig. 4.20 1D spatial projection results after rotating the phantom 90 degrees clockwise.

Directional 1D Imaging of Water Bottle Sample

To evaluate the spatial response and signal clarity along different orientations, the water bottle sample was imaged under 1D projection along the X, Y, and Z directions. As shown in Fig. 4.21, all spectrum exhibit clear peaks after applying exponential windowing and frequency alignment. Notably, the signal-to-noise ratio (SNR) was substantially improved across all directions:

- **X-axis**: from 6.63 dB (raw) to **17.64 dB**
- **Y-axis**: from 14.58 dB to **23.54 dB**
- **Z-axis**: from 8.39 dB to **24.05 dB**

In the experiments, frequency drift was consistently observed across the X, Y, and Z acquisition directions, as shown by the gray dashed curves in Fig. 4.21, which represent the Fourier-transformed signals before filtering and correction. To address this issue, a frequency shift was applied directly in the time domain by multiplying the windowed complex FID signals with a complex exponential phase factor according to:

$$S_{\text{corrected}}(t) = S_{\text{windowed}}(t) \times e^{i2\pi\Delta f t}, \tag{4.4}$$

where $S_{\text{windowed}}(t)$ represents the complex FID signal after applying an exponential decay window, Δf is the measured frequency drift for each direction, and t is the sampling time vector. In this study, the applied correction values were $\Delta f = -3.5$ Hz for the X

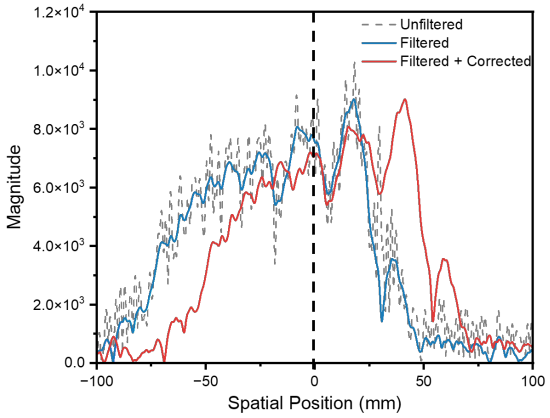

(a) Spatial spectrum along X-axis

(b) Sample orientation: X-axis

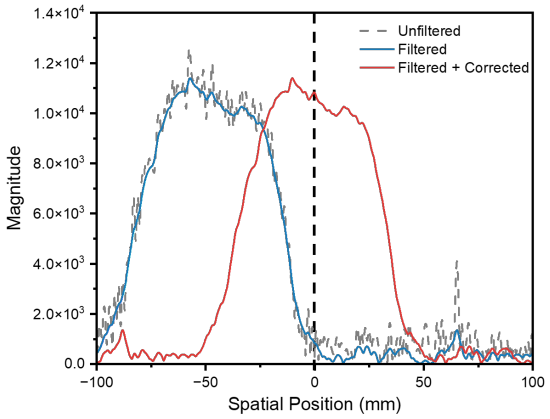

(c) Spatial spectrum along Y-axis

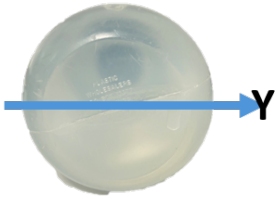

(d) Sample orientation: Y-axis

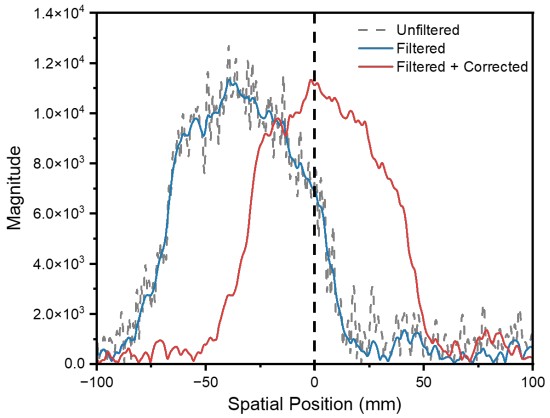

(e) Spatial spectrum along Z-axis

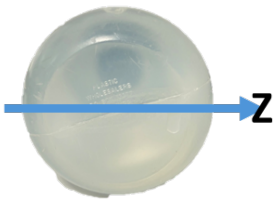

(f) Sample orientation: Z-axis

Fig. 4.21 1D EF-MRI results of the water bottle along the X, Y, and Z axes. Left: spatial frequency spectra; Right: corresponding sample orientations.

direction, $\Delta f = -9$ Hz for the Y direction, and $\Delta f = -12$ Hz for the Z direction, with negative values chosen to counteract the observed drift.

This procedure effectively realigned the frequency spectra to their theoretical center positions, thereby restoring the spatial alignment of the reconstructed images and improving the symmetry of the signal peaks in the frequency domain, as illustrated by the red curves. Frequency drift correction was essential to ensuring consistent spatial positioning across repeated acquisitions and orientations while reducing artifacts caused by environmental field fluctuations, thereby improving the signal-to-noise ratio within the regions of interest and enhancing the robustness of the reconstructed images.

4.4 2D EF-MRI: Experimental Implementation and Analysis

With the 1D projection results confirming improved SNR and spatial accuracy, the processing pipeline is next applied to 2D imaging.

Image Reconstruction Workflow

Spatial image reconstruction from time-domain FID signals in Earth's Field MRI (EF-MRI) is achieved through a structured signal processing pipeline.

- **Time-domain filtering**: An exponential decay filter is applied to suppress trailing noise in the FID signal.
- **Fourier transformation**: Each filtered signal is transformed to the frequency domain via FFT, yielding a 1D spatial projection per angle.
- **Frequency correction**: Drift across angles is compensated by aligning the spectra to a reference peak.
- **Sinogram construction**: The 1D projections are arranged by projection angle to form a sinogram.
- **FBP reconstruction**: A 2D image is obtained using filtered backprojection with appropriate frequency-domain filtering.

The sinogram generated from the aligned projections and the corresponding reconstruction filter responses are shown in Fig. 4.22. The sinogram encodes angular frequency content and serves as input to the FBP algorithm. Reconstruction quality is strongly

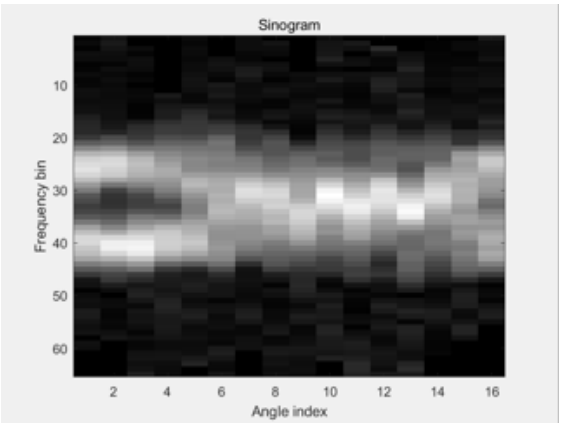

(a) Sinogram from frequency-domain projections

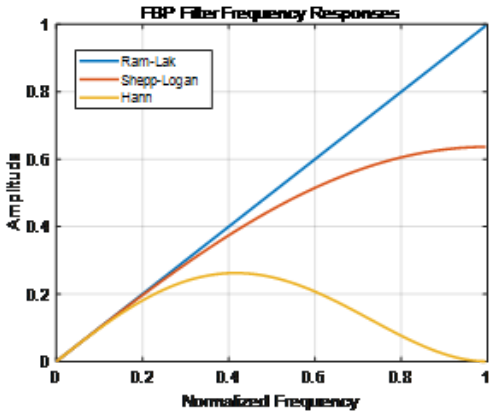

(b) Frequency responses of Ram-Lak, Shepp-Logan, and Hann filters

Fig. 4.22 (a) Sinogram constructed from aligned 1D projections; (b) Comparison of commonly used filters in FBP reconstruction.

influenced by the choice of filtering function. While the Ram-Lak filter preserves high-frequency detail, the Hann filter aggressively suppresses high frequencies, thereby reducing noise at the cost of resolution.

Image Reconstruction Results

Figure 4.23 presents 2D images reconstructed using the built-in Prospa software provided by Magritek, corresponding to the XY and XZ planes of the two-vial phantom under study. While the general outline of the phantom is faintly discernible, the reconstructed images exhibit substantial limitations in terms of image quality. High levels of background noise are apparent throughout the field of view, accompanied by poor contrast that obscures the boundaries between the phantom and the surrounding background. Additionally, the images display fuzzy edges with a lack of clear structural delineation, making it challenging to accurately identify the geometry of the vials or any fine structural details within the phantom. These issues are further exacerbated by artifacts arising from insufficient frequency correction and the absence of advanced signal preprocessing in the default reconstruction pipeline. Consequently, the spatial resolution of the Prospa-reconstructed images is significantly reduced, underscoring the need for improved preprocessing and tailored reconstruction techniques to enhance image clarity and accuracy in EF-MRI experiments.

In contrast, the bottom row presents the corresponding reconstruction results from our custom pipeline, which significantly enhances contrast and clarity.For instance, the

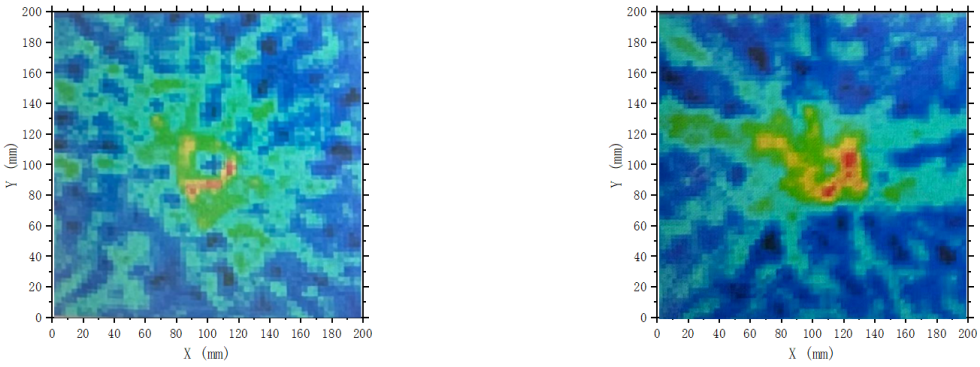

(a) XY-view (b) XZ-view

Fig. 4.23 Automatic reconstruction results from Prospa software in XY and XZ planes.

YZ-view (Fig.4.24a) demonstrates a clearer central structure with reduced peripheral noise, while the XZ-view (Fig.4.24f) reveals a more coherent object shape.

To quantitatively assess image quality, we computed the Signal-to-Noise Ratio (SNR) using a localized box-based method. As shown in Fig.4.24, our method achieves significantly improved SNR values (e.g. 39.34 dB in the YZ plane), demonstrating its effectiveness in suppressing background noise and enhancing spatial definition.

Effect of Filter Selection on Reconstruction(YZ-Plane)

Filtered backprojection (FBP) reconstructions using four distinct filters—Hann, Shepp-Logan, Ram-Lak, and no filter—are presented in Fig.**??** for the water bottle sample and in Fig.**??** for the two-vial phantom. Each filtering strategy manifests a characteristic trade-off between noise suppression and preservation of structural fidelity.

In Fig. 4.25 (Left), the reconstruction of the water bottle using the Hann filter yields a smoothly varying image with effective noise suppression; however, it compromises spatial resolution, particularly attenuating fine structural details. The Shepp-Logan and Ram-Lak filters progressively enhance edge sharpness and high-frequency content, but at the expense of elevated background noise. The unfiltered reconstruction exhibits the highest apparent signal intensity and signal-to-noise ratio (SNR), yet suffers from diminished spatial contrast, leading to the loss of anatomical delineation.

In Fig. 4.25 (Right), the differences among filters are more pronounced. The Hann-filtered image resolves both vials but with reduced intensity and edge clarity. In contrast, the Shepp-Logan and Ram-Lak filters provide sharper structural definition, though they introduce noticeable high-frequency artifacts and noise. The unfiltered result, while

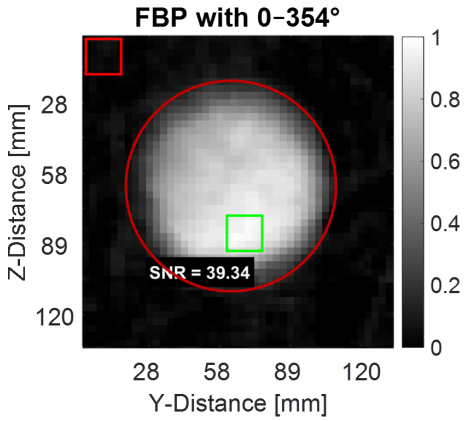

(a) YZ: Reconstructed

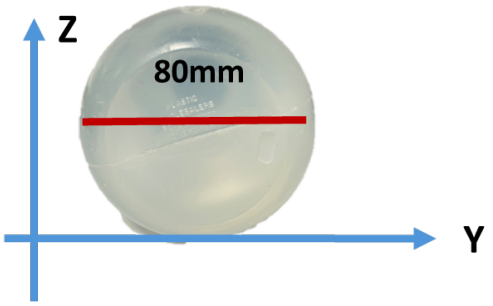

(b) YZ: Physical

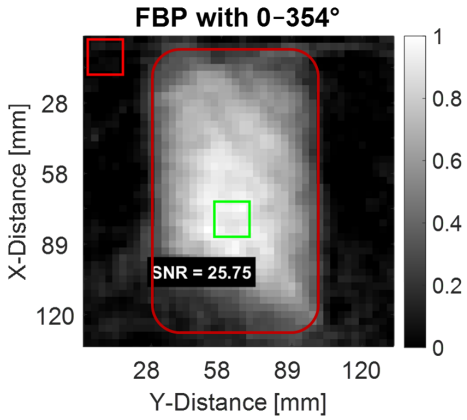

(c) YX: Reconstructed

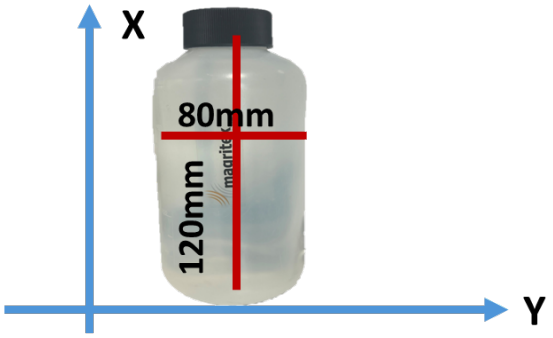

(d) YX: Physical

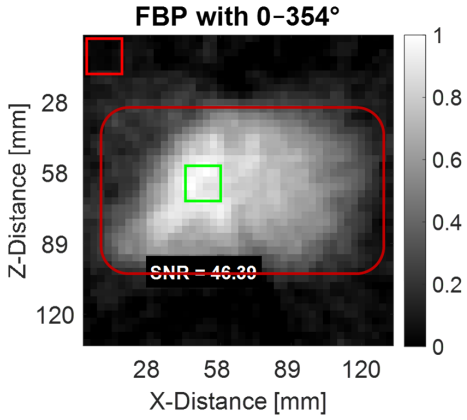

(e) XZ: Reconstructed

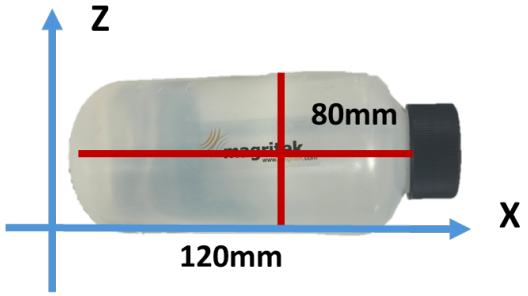

(f) XZ: Physical

Fig. 4.24 Comparison of reconstructed and physical images in three orthogonal planes (YZ, YX, and XZ). For each plane, the reconstructed image (left) and the corresponding physical orientation (right) are shown side by side for clarity.

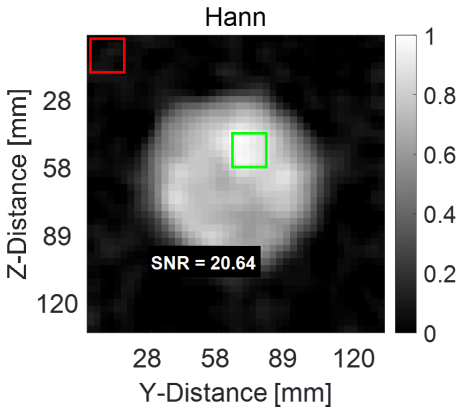

(a) Hann (Water Bottle)

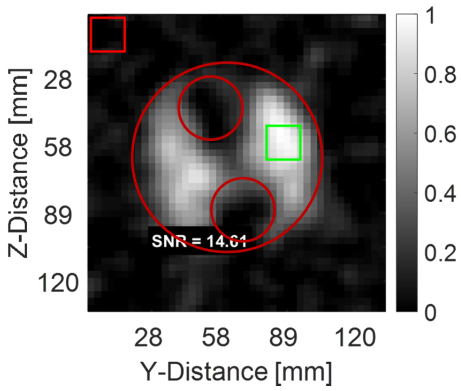

(b) Hann (Phantom)

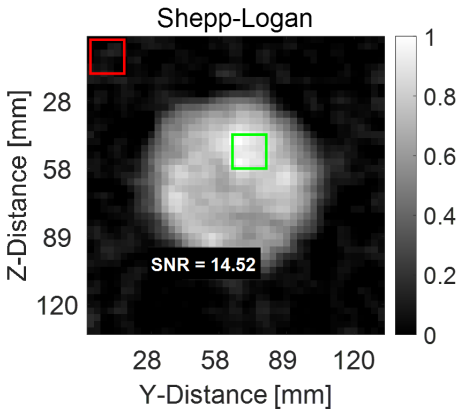

(c) Shepp-Logan (Water Bottle)

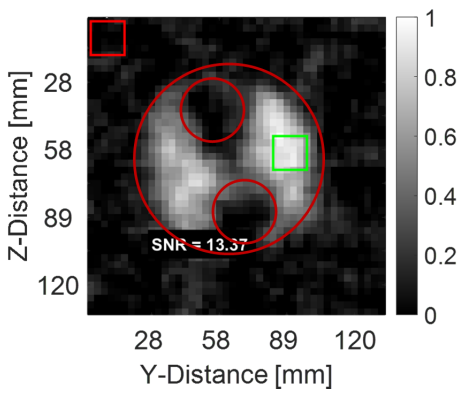

(d) Shepp-Logan (Phantom)

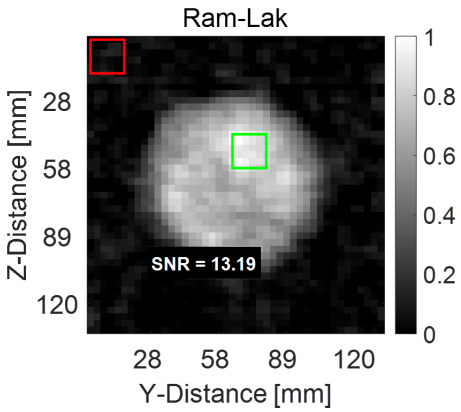

(e) Ram-Lak (Water Bottle)

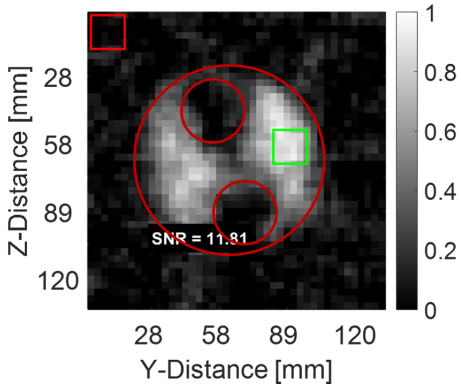

(f) Ram-Lak (Phantom)

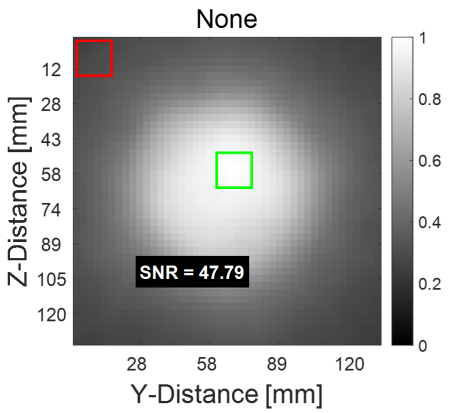

(g) No Filter (Water Bottle)

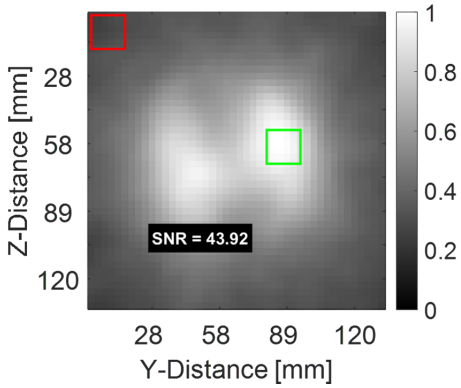

(h) No Filter (Phantom)

Fig. 4.25 Filtered backprojection $Y-Z$ reconstructions using different filters.

producing strong central signal intensity, shows excessive smoothing near the boundaries and exhibits central bias, which may obscure object separability and spatial interpretation.

These findings reinforce that high-pass filters such as Ram-Lak and Shepp-Logan are advantageous for preserving high-frequency spatial information, yet inherently amplify noise. The Hann filter offers superior noise attenuation but at the cost of edge blurring. Unfiltered FBP may yield inflated SNR estimates but is unsuitable in contexts where accurate boundary definition and feature discrimination are critical.

4.5 3D EF-MRI: Experimental Implementation and Analysis

4.5.1 Experimental Setup

To implement three-dimensional Earth's Field Magnetic Resonance Imaging (3D EF-MRI), we conducted experiments in the Blanchardstown suburb of Dublin, Ireland, using the Magritek Terranova EFNMR system under a local geomagnetic field of approximately 50 μT. The phantom consisted of a water-filled plastic bottle aligned with the Earth's field direction, as shown in Fig. 4.26, ensuring optimal signal detection during pre-polarization, excitation, and signal acquisition phases.

(a) Side view with aligned coordinate axes. (b) Front view indicating Y and Z directions.

Fig. 4.26 Water phantom positioning for 3D EF-MRI experiments at Blanchardstown.

The system employed a pre-polarization field of 7 mT applied for 3000 ms, followed by a rapid switch-off to enable nuclear spin precession in the Earth's field, with B_1 excitation pulses applied at the Larmor frequency of 2.19 kHz. Data acquisition was performed using a gradient-echo sequence with phase encoding along the Y and Z directions and readout along the X direction to achieve full three-dimensional spatial encoding.

Table 4.3 Experimental Parameters for 3D EF-MRI Acquisition at Blanchardstown

Parameter	Value
Location	Blanchardstown, Dublin, Ireland
System	Magritek Terranova EFNMR
Earth's field strength	50 μT
Pre-polarization field	7 mT
Pre-polarization duration	3000 ms
B_1 frequency	2.19 kHz
Acquisition bandwidth	32 Hz
Repetition time (TR)	10 s
Field of view (FOV)	$320 \times 320 \times 320$ mm^3
Matrix size	$64 \times 64 \times 16$
Voxel size	$4 \times 4 \times 20$ mm^3

Table 4.3 summarises the acquisition parameters for the 3D EF-MRI experiments.

4.5.2 Ideal Imaging Expectation

Under ideal conditions with a homogeneous field and stable low-noise environment, 3D EF-MRI should yield clear volumetric reconstructions of the water phantom with uniform signal intensity and accurate spatial encoding across all axes (Fig. 4.27). The k-space data are expected to be well-centered and symmetric, producing circular cross-sections in the XY and YZ planes consistent with the phantom geometry, with minimal phase errors and negligible signal voids.

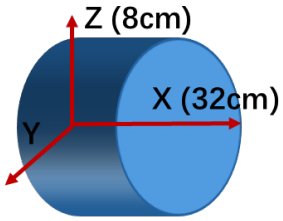

Fig. 4.27 Idealized 3D EF-MRI geometry of the cylindrical water phantom (8 cm diameter, 32 cm length).

4.5.3 Experiment Result and Analysis

Since the 3D imaging employed the k-space acquisition methodology described in the Methodology section, the MRI raw data are no longer presented as time-domain FID

signals but are directly acquired and stored as frequency-domain (k-space) data matrices. In this approach, each phase-encoding step corresponds to a specific row (or column) in k-space, while the readout direction rapidly fills the other dimension. This acquisition strategy not only improves spectral sampling efficiency but also simplifies the subsequent reconstruction process, allowing for direct spatial-domain image reconstruction from k-space via fast Fourier transform (FFT) immediately after acquisition. This methodology enabled us to directly apply signal preprocessing techniques—such as filtering, frequency drift correction, and zero-padding—on the acquired k-space data, followed by multi-dimensional FFT for rapid reconstruction of high-resolution 3D spatial images. Additionally, this flexible processing pipeline allowed us to adjust the spatial sampling resolution and FOV to align with specific experimental requirements, providing a robust foundation for subsequent SNR enhancement, image quality evaluation, and comparative analyses.

To enable high-quality image reconstruction, the acquired 3D k-space data undergoes a systematic pre-processing workflow consisting of zero-padding followed by 3D Gaussian filtering.

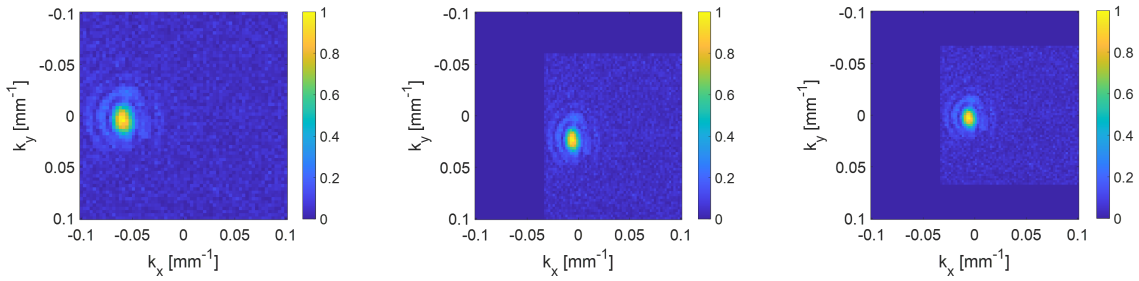

(a) Raw k-space data (64×64). (b) k-space (80×96). (c) k-space (96×96).

Fig. 4.28 Progression of zero-padding applied to k-space data. (a) Raw k-space matrix of size 64×64. (b) Intermediate zero-padding to 80×96 to center the low-frequency content. (c) Final zero-padding to 96×96 for consistent dimension alignment before filtering and reconstruction.

The initial raw k-space dataset, denoted as $\mathscr{K}_{\text{raw}}(k_x, k_y, k_z)$, has a matrix size of 64 × 64 × 16(Fig. 4.28a). To maintain the original field of view while improving effective spatial resolution, zero-padding is applied symmetrically along the k_x and k_y axes, expanding the matrix to 96 × 96 × 16(Fig. 4.28c). Importantly, this zero-padding operation re-centers the essential low-frequency k-space information, which is initially located at the lower-left corner due to acquisition ordering, into the center of the frequency domain. This re-centering is critical as it facilitates the application of frequency-domain filtering and subsequent processing steps, ensuring that the filtering operations are aligned with the

principal energy regions of the data. Additionally, the increased sampling density in the frequency domain resulting from zero-padding allows for smoother interpolation during inverse Fourier transformation while preserving the physical field of view, thereby supporting artifact-free reconstruction in the subsequent processing stages.

Following zero-padding, 3D Gaussian filtering is employed to attenuate high-frequency noise while preserving low-frequency components containing essential spatial structure information (Fig. 4.29). The Gaussian filter in each dimension is defined as:

$$G(k) = \exp\left(-\frac{k^2}{2\sigma^2}\right),$$

where k denotes the frequency variable in the respective dimension, and σ determines the filter's bandwidth. The filter is constructed to match the padded k-space dimensions and is applied multiplicatively across all axes:

$$\mathcal{K}_{\text{filtered}}(k_x, k_y, k_z) = G_{k_x}(k_x) \cdot G_{k_y}(k_y) \cdot G_{k_z}(k_z) \cdot \mathcal{K}_{\text{padded}}(k_x, k_y, k_z).$$

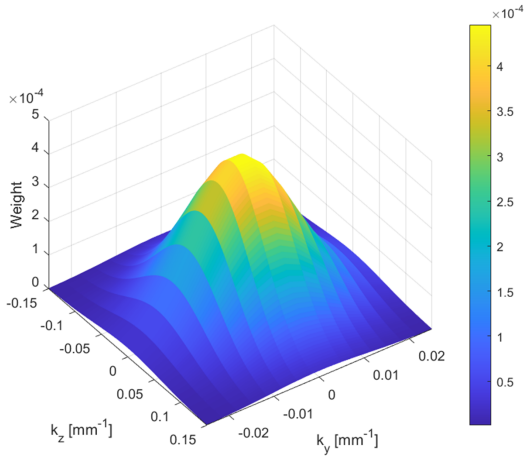

Fig. 4.29 Three-dimensional Gaussian filter in the k_y-k_z plane used for k-space filtering.

This isotropic filtering strategy attenuates noise-dominant high-frequency components while preserving signal-dominant low-frequency regions crucial for accurate spatial representation.

The rationale for this processing pipeline is based on balancing the trade-off between spatial resolution and noise suppression, which is particularly critical in low-field MRI applications where SNR is inherently limited. By appropriately tuning the Gaussian

bandwidth, the filtering process optimizes this balance, ensuring that structural details are retained while background noise is significantly reduced.

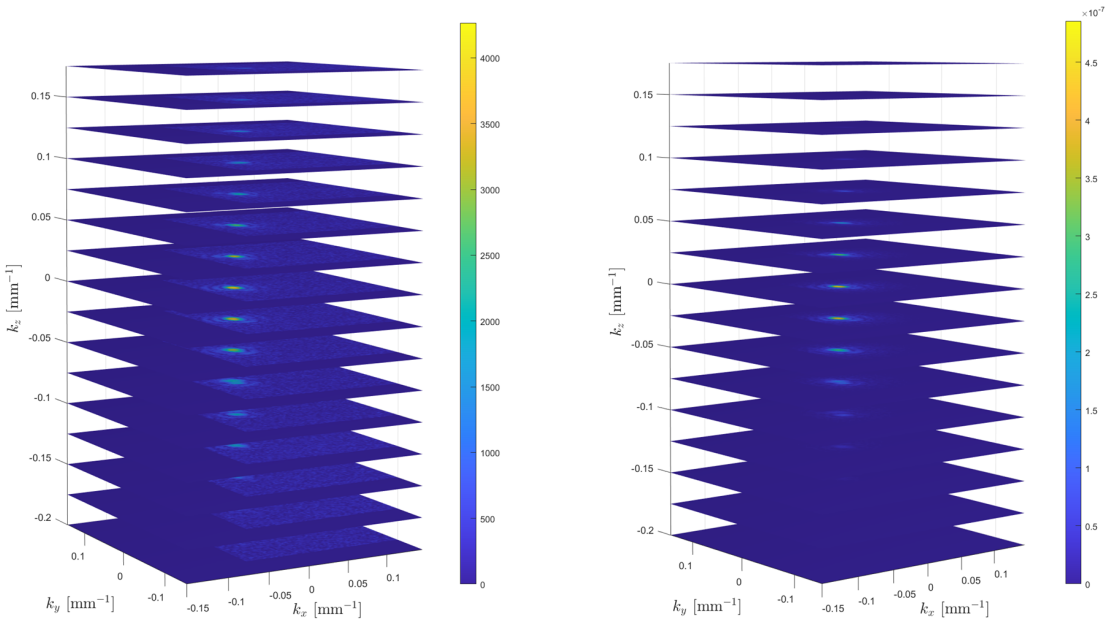

(a) Stacked k-space data before filtering.

(b) Stacked k-space data after applying a 3D Gaussian filter.

Fig. 4.30 Comparison of stacked k-space slices before and after 3D Gaussian filtering 64x64x16 acquisition. Filtering improves the effective SNR and suppresses high-frequency artifacts while retaining essential signal components for accurate reconstruction.

As shown in Fig. 4.30, the processed k-space data transitions from a compact, noisy representation to a smoother, denoised distribution suitable for subsequent inverse Fourier transform reconstruction. This preparation ensures that the reconstructed images exhibit enhanced clarity, reduced artifacts, and improved interpretability, facilitating further quantitative and qualitative analyses.

Following k-space filtering and zero-padding, a 3D inverse Fourier transform (IFFT) was applied to reconstruct spatial-domain images from the processed k-space data. Figure 4.31 presents a direct comparison of the reconstructed slices (Slices 9–12) before and after Gaussian filtering.

The top panel shows the reconstructed slices from the unfiltered k-space, where the object structure is partially visible, but the images exhibit high background noise and blurred boundaries, leading to limited contrast and reduced clarity of the phantom edges. In contrast, the bottom panel displays the reconstructed slices after 3D Gaussian filtering,

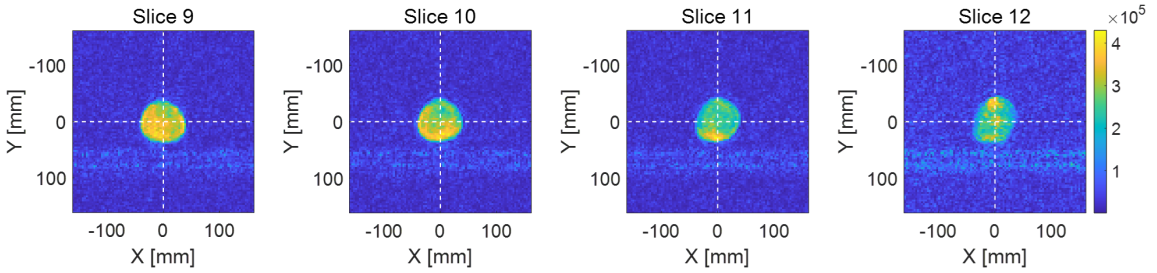

(a) Before filtering

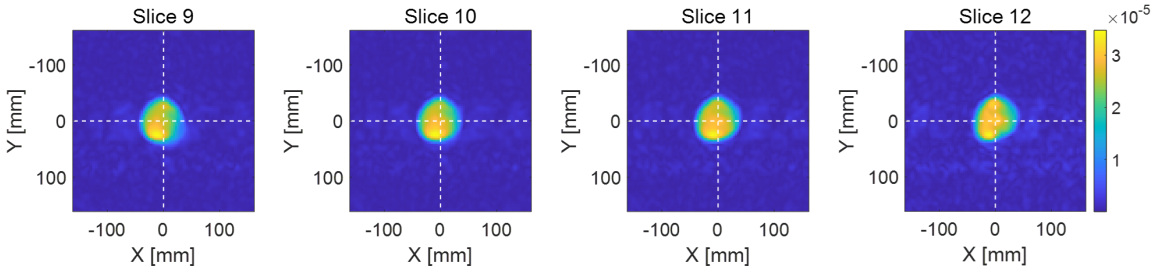

(b) After filtering

Fig. 4.31 Reconstructed images of slices 9–12 before and after k-space filtering. Filtering suppresses noise and enhances structural boundaries, facilitating clearer visualization in filtered backprojection reconstructions.

where a noticeable improvement in image quality is observed. The noise level in the background is significantly reduced, and the edges of the phantom become sharper and more continuous across slices.

To quantitatively evaluate the denoising performance of *k*-space filtering on the reconstructed MRI slices, an automatic signal-to-noise ratio (SNR) calculation method was implemented. Figure 4.32 illustrates the SNR maps and corresponding histograms before and after *k*-space filtering.

The reconstructed images were first normalized and displayed to facilitate consistent comparisons across different processing conditions. To automate region-of-interest (ROI) selection for SNR calculation, a threshold-based segmentation was applied. Specifically, pixels with intensity values greater than 0.2 were classified as the signal region, while pixels with values below 0.05 were considered as the background region. These thresholds were selected empirically based on histogram distributions to ensure robust separation between signal and background components while avoiding the inclusion of noise or partial volume artifacts within the signal ROI.

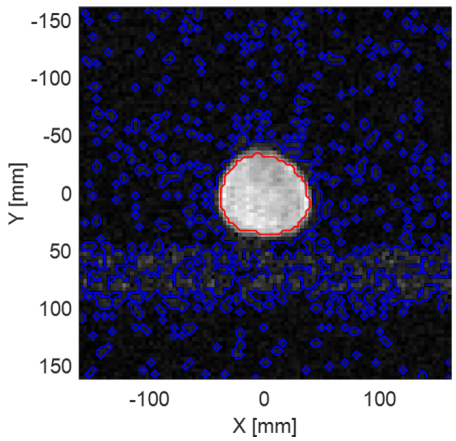

(a) SNR visualization before filtering

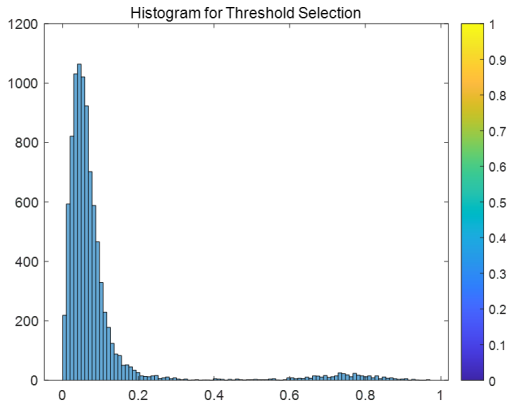

(b) Histogram before filtering

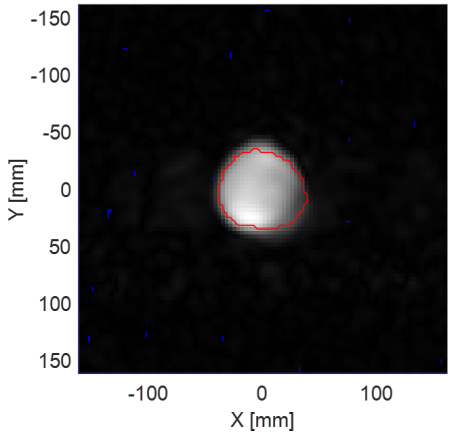

(c) SNR visualization after filtering

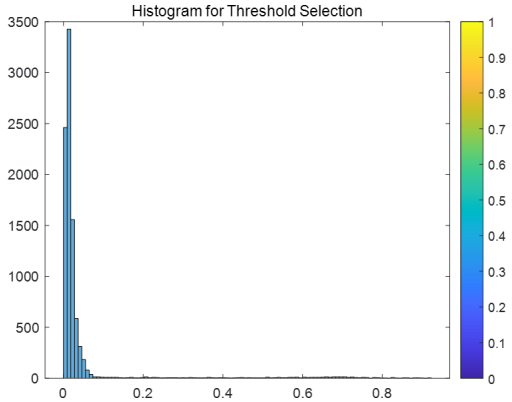

(d) Histogram after filtering

Fig. 4.32 Quantitative evaluation of denoising performance before and after k-space filtering using automated SNR calculation and histogram-based ROI segmentation.

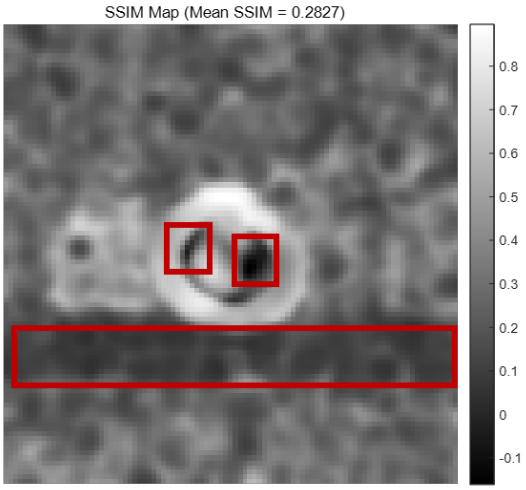

Fig. 4.33 SSIM Map

The mean signal value was computed over the signal mask, and the noise standard deviation was calculated from the background mask. The SNR was then defined as:

$$\text{SNR} = \frac{\mu_{\text{signal}}}{\sigma_{\text{noise}}} \tag{4.5}$$

where μ_{signal} denotes the mean signal intensity, and σ_{noise} represents the standard deviation of the background noise.

In addition, the structural similarity index (SSIM) between the filtered and unfiltered reconstructed images was computed to assess the preservation of structural information after filtering. The SSIM map highlights localized structural differences, while the mean SSIM value provides an overall assessment of structural fidelity.

Figure 4.33 presents the Structural Similarity Index (SSIM) map between the filtered and unfiltered EF-MRI reconstructed slices, evaluating the local structural consistency after applying the 3D Gaussian filtering procedure. The SSIM values are displayed on a normalized grayscale colormap, where brighter regions indicate higher similarity and darker regions indicate lower similarity.

The highlighted red regions in the figure correspond to areas where significant differences between the filtered and unfiltered images are observed, reflected in lower SSIM values. Notably, the large rectangular region at the bottom aligns with the noise band typically present in unfiltered reconstructions. The reduced SSIM in this region indicates that the filtering process effectively suppresses noise components, resulting in the removal of non-structural artifacts from the reconstruction.

Similarly, the two smaller red boxes within the phantom region indicate areas where the filtering procedure has modified the image content compared to the unfiltered reconstruction. These changes, however, do not indicate a loss of true structural information; instead, they represent the attenuation of noise superimposed on the underlying signal, allowing the true anatomical structures within the vials to emerge more distinctly in the filtered reconstruction.

Overall, the SSIM map confirms that the 3D Gaussian filtering selectively reduces noise while preserving and enhancing the visibility of the true structural information within the EF-MRI data, thereby improving the reliability of subsequent quantitative and qualitative analyses. This automated pipeline ensures consistent and reproducible quantitative evaluation of denoising performance and structural preservation across different filtering parameters in k-space, supporting objective comparisons during filter optimization.

This improvement demonstrates the effectiveness of 3D Gaussian filtering in suppressing high-frequency noise while preserving essential structural information in EF-MRI, thereby enabling more reliable spatial localization and improved visual interpretation in ultra-low field MRI imaging pipelines.

CHAPTER 5

Conclusion and Future Work

This thesis has explored the implementation of Earth's Field Magnetic Resonance Imaging (EF-MRI) under urban environmental conditions, systematically addressing the challenges associated with low-field imaging while enhancing signal fidelity through optimized acquisition and advanced signal processing techniques.

A comprehensive experimental workflow was established, spanning 1D, 2D, and 3D EF-MRI acquisitions on phantom models. Through decay windowing, zero-padding, and frequency correction, followed by k-space Gaussian filtering, the effective signal-to-noise ratio (SNR) was significantly improved while retaining spatial resolution across reconstructed images. Results demonstrated that despite the limitations imposed by ultra-low field strengths—including low intrinsic polarization, environmental electromagnetic interference, and magnetic field inhomogeneities—EF-MRI can consistently produce spatially resolved images with interpretable structural features, underscoring its viability as a cost-effective and portable imaging modality.

However, challenges remain that limit the practical deployment of EF-MRI systems. A persistent issue in urban EF-MRI is frequency drift in the Earth's magnetic field during data acquisition, which can induce phase inconsistencies and spatial blurring in k-space and subsequently degrade image quality. Conventional frequency correction strategies, often applied globally in the time domain, may be insufficient in scenarios with temporally varying or localized perturbations in the field.

Future work will focus on developing advanced k-space frequency drift compensation methods. This may involve real-time frequency tracking during acquisition using

reference FID signals embedded within the acquisition protocol or retrospective phase correction algorithms applied in k-space by estimating frequency drift trajectories slice-by-slice and line-by-line. Techniques such as k-space navigator echoes or phase-stabilized reference scans could be leveraged to dynamically adjust for frequency drift during 3D acquisitions, mitigating phase inconsistencies without prolonging scan times.

Additionally, advanced signal processing strategies will be explored to further enhance EF-MRI reconstruction quality. PCA-based denoising, low-rank matrix recovery, and compressed sensing reconstruction pipelines can be integrated into the EF-MRI workflow to suppress noise while preserving structural fidelity in low-SNR datasets. The application of deep-learning-assisted reconstruction techniques may offer further improvements by learning data-driven priors that enhance image quality even under highly undersampled or noisy conditions.

On the hardware side, future efforts will include the investigation of multi-channel receiver coils to improve sensitivity and reduce acquisition time, while maintaining spatial resolution for 3D imaging. Combined with advanced reconstruction methods, this will enable the translation of EF-MRI systems toward practical use in community health screening and low-resource clinical settings.

Finally, extending the EF-MRI system for in vivo imaging in human studies under real-world conditions will be a critical step toward validating the modality's diagnostic potential. Long-term goals will focus on the integration of EF-MRI with hybrid portable diagnostic platforms, contributing to the democratization of medical imaging technologies and expanding the accessibility of MRI to underserved regions globally.

References

[1] O Denisova, V Sapunov, and A Denisov. Influence of magnetic field variations on measurements by magnetometers using averaging algorithms. *Earth, planets and space*, 58:731–734, 2006.

[2] Georges J Béné. Nuclear magnetism of liquid systems in the earth field range. *Physics Reports*, 58(4):213–267, 1980.

[3] Paul C Lauterbur. Image formation by induced local interactions: examples employing nuclear magnetic resonance. *nature*, 242(5394):190–191, 1973.

[4] Janez Stepišnik, Vital Eržen, and Miha Kos. Nmr imaging in the earth's magnetic field. *Magnetic resonance in medicine*, 15(3):386–391, 1990.

[5] Meghan E Halse, Andrew Coy, Robin Dykstra, Craig Eccles, Mark Hunter, Rob Ward, and Paul T Callaghan. A practical and flexible implementation of 3d mri in the earth's magnetic field. *Journal of Magnetic Resonance*, 182(1):75–83, 2006.

[6] Vadim S Zotev, Andrei N Matlachov, Petr L Volegov, Henrik J Sandin, Michelle A Espy, John C Mosher, Algis V Urbaitis, Shaun G Newman, and Robert H Kraus. Multichannel squid system for meg and ultra-low-field mri. *IEEE transactions on applied superconductivity*, 17(2):839–842, 2007.

[7] Friedrich Wetterling, Conor Conway, Shane Hunt, Arun Bokde, and Anil Kokaram. Ultra-low field magnetic resonance imaging of the human forearm in the earth's magnetic field of dublin, ireland. In *Proceedings of the British and Irish Chapter of the International Society for Magnetic Resonance in Medicine*, pages 98–99, Nottingham, UK, 2024.

[8] Gary Liney. *MRI in Clinical Practice*. Springer Science & Business Media, Cham, Switzerland, 2007.

[9] Charles G Fry. The nobel prize in medicine for magnetic resonance imaging, 2004.

[10] World Health Organization et al. *Atlas: Multiple Sclerosis Resources in the World*. World Health Organization, Geneva, Switzerland, 2008.

[11] OECD. Number of magnetic resonance imaging (mri) units in selected countries as of 2016 (per million population). https://www.statista.com/statistics/282401/density-of-magnetic-resonance-imagingunits-by-country/, 2016. Accessed: 2025-06-18.

[12] Paul Browne, Dhia Chandraratna, Ceri Angood, Helen Tremlett, Chris Baker, Bruce V Taylor, and Alan J Thompson. Atlas of multiple sclerosis 2013: a growing global problem with widespread inequity. *Neurology*, 83(11):1022–1024, 2014.

[13] Franco Servadei, Zefferino Rossini, Federico Nicolosi, Carlotta Morselli, and Kee B Park. The role of neurosurgery in countries with limited facilities: facts and challenges. *World neurosurgery*, 112:315–321, 2018.

[14] Adrian Burton. Training non-physicians as neurosurgeons in sub-saharan africa. *The Lancet Neurology*, 16(9):684–685, 2017.

[15] Technopak. Technopak healthcare outlook. http://www.technopak.com/files/Outlook_Oncology.pdf, 2011. Accessed: 2025-06-18.

[16] Esteban Anoardo and Gonzalo G Rodriguez. New challenges and opportunities for low-field mri. *Journal of Magnetic Resonance Open*, 14:100086, 2023.

[17] PT Callaghan, A Coy, R Dykstra, CD Eccles, ME Halse, MW Hunter, OR Mercier, and JN Robinson. New zealand developments in earth's field nmr. *Applied Magnetic Resonance*, 32:63–74, 2007.

[18] Yilong Liu, Alex TL Leong, Yujiao Zhao, Linfang Xiao, Henry KF Mak, Anderson Chun On Tsang, Gary KK Lau, Gilberto KK Leung, and Ed X Wu. A low-cost and shielding-free ultra-low-field brain mri scanner. *Nature communications*, 12(1):7238, 2021.

[19] John C Fortney, James F Burgess, Hayden B Bosworth, Brenda M Booth, and Peter J Kaboli. A re-conceptualization of access for 21st century healthcare. *Journal of general internal medicine*, 26:639–647, 2011.

[20] M Packard. Free nuclear induction in earth's magnetic field. *Phys. Rev.*, 93:941, 1954.

[21] GS Waters. A measurement of the earth's magnetic field by nuclear induction. *Nature*, 176(4484):691–691, 1955.

[22] Peter Mansfield and Peter K Grannell. Nmr'diffraction'in solids? *Journal of Physics C: solid state physics*, 6(22):L422, 1973.

[23] U Skalerič, J Dolinšek, J Stepisnik, P Cevc, and M Schara. Nmr imaging in dentistry: relaxation and diffusion studies. *Advances in Dental Research*, 1(1):85–87, 1987.

[24] Steffen Lother, Uvo Hoelscher, Thomas Kampf, Peter Jakob, and Florian Fidler. 3d gradient system for two b 0 field directions in earth's field mri. *Magnetic Resonance Materials in Physics, Biology and Medicine*, 26:565–573, 2013.

[25] Erwin L Hahn. Spin echoes. *Physical review*, 80(4):580, 1950.

[26] Herman Y Carr and Edward M Purcell. Effects of diffusion on free precession in nuclear magnetic resonance experiments. *Physical review*, 94(3):630, 1954.

[27] PT Callaghan, CD Eccles, TG Haskell, PJ Langhorne, and JD Seymour. Earth's field nmr in antarctica: a pulsed gradient spin echo nmr study of restricted diffusion in sea ice. *Journal of Magnetic Resonance*, 133(1):148–154, 1998.

[28] MW Hunter, R Dykstra, MH Lim, TG Haskell, and PT Callaghan. Using earth's field nmr to study brine content in antarctic sea ice: comparison with salinity and temperature estimates. *Applied Magnetic Resonance*, 36:1–8, 2009.

[29] PT Callaghan, CD Eccles, and JD Seymour. An earth's field nuclear magnetic resonance apparatus suitable for pulsed gradient spin echo measurements of self-diffusion under antarctic conditions. *Review of scientific instruments*, 68(11):4263–4270, 1997.

[30] PT Callaghan, R Dykstra, CD Eccles, TG Haskell, and JD Seymour. A nuclear magnetic resonance study of antarctic sea ice brine diffusivity. *Cold Regions Science and Technology*, 29(2):153–171, 1999.

[31] DV Trushkin, OA Shushakov, and AV Legchenko. The potential of a noise-reducing antenna for surface nmr ground-water surveys in the earth's magnetic field. *Geophysical Prospecting*, 42(8):855–862, 1994.

[32] Oleg A Shushakov. Groundwater nmr in conductive water. *Geophysics*, 61(4):998–1006, 1996.

[33] Kevin N Sheth, Mercy H Mazurek, Matthew M Yuen, Bradley A Cahn, Jill T Shah, Adrienne Ward, Jennifer A Kim, Emily J Gilmore, Guido J Falcone, Nils Petersen, et al. Assessment of brain injury using portable, low-field magnetic resonance imaging at the bedside of critically ill patients. *JAMA neurology*, 78(1):41–47, 2021.

[34] Friedrich Wetterling, Martin Tabbert, Sven Junge, Lindsay Gallagher, I Mhairi Macrae, and Andrew J Fagan. A double-tuned 1h/23na dual resonator system for tissue sodium concentration measurements in the rat brain via na-mri. *Physics in Medicine & Biology*, 55(24):7681–7695, 2010.

[35] Friedrich Wetterling, Dominique M Corteville, Raffi Kalayciyan, Andreas Rennings, Simon Konstandin, Armin M Nagel, Helmut Stark, and Lothar R Schad. Whole body sodium mri at 3t using an asymmetric birdcage resonator and short echo time sequence: first images of a male volunteer. *Physics in Medicine & Biology*, 57(14):4555, 2012.

[36] Charles P Slichter. *Principles of magnetic resonance*, volume 1. Springer Science & Business Media, 2013.

[37] Anatole Abragam and Maurice Goldman. Nuclear magnetism: order and disorder. 1982.

[38] E Hiltbrand, B Borcard, R Sechehaye, and GJ Bene. Frequency shifts in nuclear spin system. *Helv. Phys. Acta;(Switzerland)*, 49(2), 1976.

[39] William Happer. Optical pumping. *Reviews of modern physics*, 44(2):169, 1972.

[40] Harold Weinstock and Appliations. *SQUID sensors : fundamentals, fabrication, and applications*. 1996.

[41] Ya S Greenberg. Application of superconducting quantum interference devices to nuclear magnetic resonance. *Reviews of Modern Physics*, 70(1):175, 1998.

[42] HC Seton, JMS Hutchison, and DM Bussell. A 4.2 k receiver coil and squid amplifier used to improve the snr of low-field magnetic resonance images of the human arm. *Measurement Science and Technology*, 8(2):198, 1997.

[43] S Kumar, BD Thorson, and WF Avrin. Broadband squid nmr with room-temperature samples. *Journal of Magnetic Resonance, Series B*, 107(3):252–259, 1995.

[44] Carl A. Michal. Low-cost low-field nmr and mri: Instrumentation and applications. *Journal of Magnetic Resonance*, 319:106800, 2020.

[45] Neil J Stewart, Laurie J Smith, Ho-Fung Chan, James A Eaden, Smitha Rajaram, Andrew J Swift, Nicholas D Weatherley, Alberto Biancardi, Guilhem J Collier, David Hughes, et al. Lung mri with hyperpolarised gases: current & future clinical perspectives. *The British Journal of Radiology*, 95(1132):20210207, 2022.

[46] Jonathan Mitchell, TC Chandrasekera, DJ Holland, LF Gladden, and EJ Fordham. Magnetic resonance imaging in laboratory petrophysical core analysis. *Physics Reports*, 526(3):165–225, 2013.

[47] WC Dickinson. Dependence of the f 19 nuclear resonance position on chemical compound. *Physical Review*, 77(5):736, 1950.

[48] Walter D Knight. Nuclear magnetic resonance shift in metals. *Physical Review*, 76(8):1259, 1949.

[49] James T Arnold, SS Dharmatti, and ME Packard. Chemical effects on nuclear induction signals from organic compounds. *The journal of chemical physics*, 19(4):507, 1951.

[50] LH Meyer, A Saika, and HS Gutowsky. Electron distribution in molecules. iii. the proton magnetic spectra of simple organic groups1. *Journal of the American Chemical Society*, 75(18):4567–4573, 1953.

[51] Michelle Espy, Shermiyah Baguisa, David Dunkerley, Per Magnelind, Andrei Matlashov, Tuba Owens, Henrik Sandin, Igor Savukov, Larry Schultz, Algis Urbaitis, et al. Progress on detection of liquid explosives using ultra-low field mri. *IEEE transactions on applied superconductivity*, 21(3):530–533, 2011.